

Recommended Practices for the Experimental Characterization of Gridded Ion Engines

IEPC-2025-690

*Presented at the 39th International Electric Propulsion Conference
Imperial College London • London, United Kingdom
14-19 September 2025*

John E. Foster¹

University of Michigan, Ann Arbor, MI, 48109, USA

Robert E. Thomas² and George C. Soulard³

NASA Glenn Research Center, Cleveland, OH, 44135, USA

John Brophy⁴

Jet Propulsion Laboratory/California Institute of Technology, Pasadena, CA, 91109, USA

Kristof Holste⁵

Justus Liebig University, DE-35392 Giessen, Germany

Daniel Spemann⁶ and Christoph Eichhorn⁷

Leibniz Institute of Surface Engineering (IOM), 04318 Leipzig, Germany

Hiroyuki Koizumi⁷

The University of Tokyo, Kashiwa, Chiba, 277-8561, Japan

Ryudo Tsukizaki⁸

JAXA

Michael Tsay⁹

Busek Co. Inc., Natick, MA, 01863, U.S.A.

Rittu S. Raju¹⁰

HX5 LLC, Cleveland, OH, 44135, USA

Tyler Topham

The University of Michigan/Turion, USA

Sophia Bergman, The University of Michigan

¹ Professor, jefoster@umich.edu

² Aerospace Engineer, robert.e.thomas@nasa.gov

³ Aerospace Engineer, george.c.soulard@nasa.gov

⁴ Engineering Fellow, john.r.brophy@jpl.nasa.gov

⁵ Senior Scientist, kristof.holste@physik.uni-giessen.de

⁶ Senior Scientist, daniel.spemann@iom-leipzig.de and christoph.eichhorn@iom-leipzig.de

⁷ Professor, koizumi@al.t.u-tokyo.ac.jp

⁸ JAXA and Associate Professor-University of Tokyo, tsukizaki.ryudo@jaxa.jp

⁹ Chief Scientist, mtsay@busek.com

¹⁰ Aerospace Engineer, ritz.s.raju@nasa.gov



Abstract: This paper provides a comprehensive overview of best practices for characterizing gridded ion engines. It is part of a series of papers designed to serve as guidebooks for the consistent operation and characterization of electric propulsion devices. Understanding and optimizing gridded ion engine performance requires effective methods for measuring operational parameters. These measurements not only offer valuable insights into engine performance, but provide the information needed for flight, as well as enabling direct, meaningful comparisons with existing literature. Additionally, this document informs modelers about the measurement methods and conditions under which performance data were obtained, providing a foundation for model validation and cross-comparison with other engine systems. Methods to characterize the engine are drawn from numerous approaches in the experimental methods sections of thruster publications as well as in texts such as that of Katz and Goebel. In this paper, we highlight key characterization procedures found in the literature and consolidate these methods into a single document. Key performance parameters and how to measure them include: 1) perveance limits, 2) neutralizer operating modes, 3) discharge losses, 4) back-streaming limits, and 5) ion transparency. This work is based on the best approaches developed by national laboratories, space agencies and universities worldwide to understand the transportability of these methods. Transportability is essential to enable comparison of measured performance characteristics from laboratories around the world. This document is intended to serve as a compact guide for those new to the field to for the implementation of best practices for experimental characterization of gridded ion engines.

Nomenclature

A	= area, m ²
f_i	= ion current fraction for the i^{th} charge state
f_p	= flatness parameter
m	= ion mass, kg
J	= total ion current, A
J_{axial}	= axial component of beam current, A
j_b	= current density, A/m ²
J_b	= beam current, A
q	= ion charge, C
r	= probe position vector, m
R_g	= grid radius, m
T	= thrust, N
V_b	= beam voltage, V
η_d	= thrust correction factor for beam divergence
η_s	= thrust correction factor for multiply charged ions
λ	= beam divergence half angle, rad
γ	= probe angle for two-point model, rad
κ	= probe correction factor
θ	= probe angle relative to thrust axis, rad



I. Introduction and Scope

Gridded ion thruster technology remains a compelling option for missions ranging from near Earth applications such as station keeping and orbit raising, high-power missions in cis-lunar space, Mars exploration missions, deep space solar system exploration missions, planetary defense missions, and even missions beyond the solar system such as NASA Origins Program for imaging Earth-like planets. This range is enabled by the high specific impulse provided by gridded ion thrusters, typically 3000 s to 4000 s for the state-of-the-practice to > 10,000 s, along with high efficiency that results from the fact that the ion acceleration process is greater than 99% efficient. An attractive feature of gridded ion thrusters is that the plasma production and ion acceleration processes are largely separable. This enables a variety of plasma production approaches to be coupled with high-performance ion accelerator systems. The three most extensively developed plasma production methods—the three that have been flown operationally in space—are: 1) the direct-current (DC) discharge ion engine; 2) the radiofrequency (RF) ion engine; and 3) the microwave electron cyclotron resonance engine.

All ion thrusters perform three basic functions: ionization of the propellant, acceleration of the resulting positive ions, and neutralization of the accelerated ion beam. These three functions are illustrated in Fig. 1 which is applicable to the vast majority of ion thruster designs regardless of the mechanism used to ionize the propellant. During normal operation, gaseous propellant (typically xenon) flows into the discharge chamber where it is ionized by DC, RF, or microwave discharges. In all three cases, the discharge chamber produces a weakly ionized, low-pressure plasma. An external high-voltage power supply is used to raise the discharge chamber plasma to a potential that is typically several hundred to a few thousand volts above the ambient space plasma potential. A fraction of the ions produced in the discharge chamber drift toward the ion accelerator system consisting of the Screen Grid and the Accelerator Grid (though a third grid can also be implemented) in Fig. 1. The ion accelerator system extracts these ions from the discharge chamber plasma and accelerates them up to a final energy that is very close to the applied positive high voltage. Electrons stripped from the propellant atoms in the ionization process are collected by the discharge chamber, go through the external positive high-voltage power supply and are routed to a neutralizer cathode which injects them into the ion beam. Proper ion thruster operation requires that the current of electrons injected into the ion beam exactly match the ion beam current.



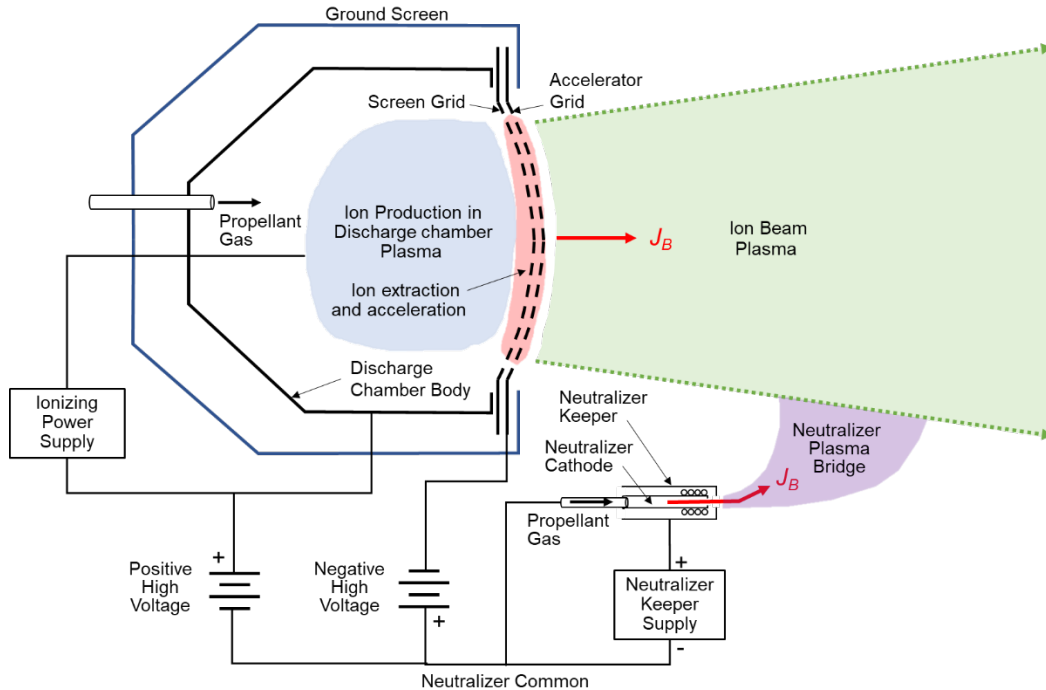


Figure 1. Illustration of ion thruster operation showing the three basic functions that all ion thrusters perform: propellant ionization, ion acceleration, and ion beam neutralization.

Most DC ion thrusters use a hollow cathode, shown in Fig. 2, for the neutralizer cathode. During normal hollow cathode operation, a secondary flow of propellant gas is required. The neutralizer cathode creates an internal plasma, that enhances electron emission, as well as an external plasma. The external plasma creates a high-conductivity path called a “plasma bridge” between the neutralizer cathode and the ion beam. This plasma bridge enables the neutralizer cathode to be located well outside of the ion beam while still enabling the conduction of amperes of electron current across the gap. Without this plasma bridge, the neutralizer cathode would have to be located at the edge of the ion beam where it would be subject to substantial erosion by the beam ions. The electrons from the neutralizer have a temperature of around 2 eV with an average speed that is much greater than the beam ions. These electrons can flow upstream toward the ion thruster. To prevent these electrons from “back-streaming” into the positively-biased, high-voltage discharge chamber, the accelerator grid is biased negative a few hundred volts. In addition, the rest of the discharge chamber is surrounded by an enclosure, called the “Ground Screen,” maintained at spacecraft ground. This structure prevents neutralizer plasma electrons from bypassing the beam and directly contacting the anode.



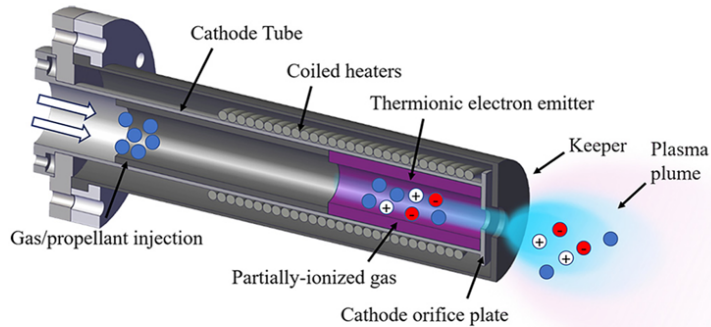


Figure 2. A typical hollow cathode configuration used in gridded ion thrusters.

The ion accelerator system is comprised of two or more closely-spaced electrodes with matching pairs of apertures. The thickness of each electrode, the size of the apertures, and the separation between the electrodes are carefully designed to extract a high fraction of the ions reaching the accelerator system and accelerate them to the required exhaust velocity while minimizing the loss of neutral propellant atoms. Since the accelerator system is full of holes and the plasma is only weakly ionized, some of the propellant leaks out of the discharge chamber unionized. This causes two problems. First, the loss of unionized propellant reduces the specific impulse and efficiency of the thruster. Second, the relatively slow-moving propellant atoms flowing between and downstream of the grids can undergo charge-exchange collisions with the fast-moving beam ions. In these collisions, an electron jumps from the neutral atom to the beam ion resulting in a fast-moving neutral atom and a slow-moving ion. Depending on where they are formed, these positively-charged, slow-moving, charge-exchange ions can get accelerated into the negatively-charged accelerator grid causing erosion by ion sputtering. This is the primary wear-out failure mode for most ion thrusters. Focusing effects typically require the accelerator grid apertures to be smaller in diameter than the screen grid apertures. The use of smaller accelerator grid apertures helps reduce the loss of unionized propellant through the grids.

To illustrate the three basic functions of ionization, acceleration and neutralization, consider the simplified circuit diagram for a direct-current (DC) ion engine in Fig. 3. The three basic functions are accomplished by just three of the power supplies in this figure, the Anode Supply, the Screen Supply, the Accelerator Supply. The other supplies are used to start the cathodes or to sustain their operation during arcing events. The anode supply provides the power to ionize the propellant. The screen supply accelerates the ions. The accelerator supply helps focus the ions through the accelerator grid and provides the negative voltage that prevents electron back-streaming. In a radio-frequency (or microwave) ion thruster, the discharge power supply is replaced by an RF (or microwave) generator and the cathode heater and keeper supplies are eliminated. The microwave engines utilize a microwave driven plasma to produce neutralizing electrons .

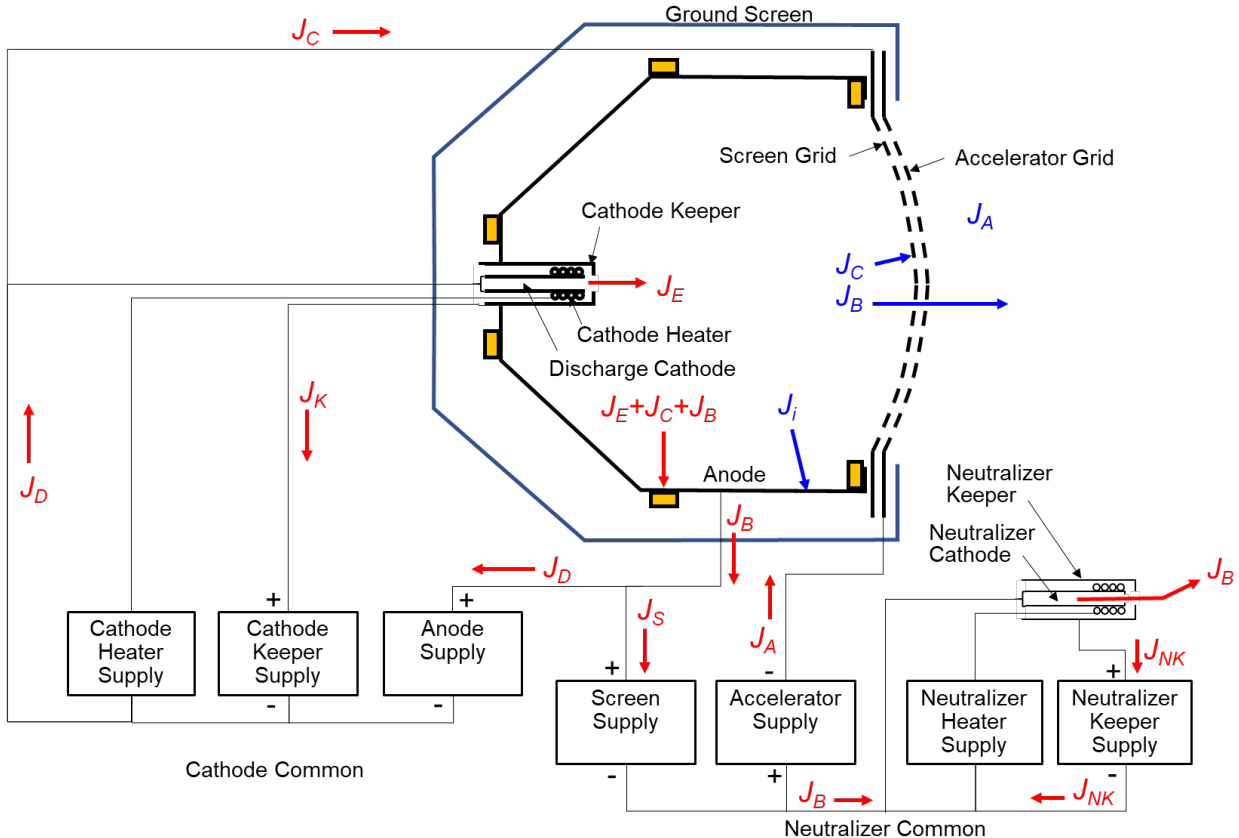


Figure 3. Simplified circuit diagram for a DC ion thruster with key currents indicated. Ion currents are shown in blue, electron currents in red. Actual currents, by convention are in the opposite direction of the flow of electrons (red arrows). The sizes of the arrows do not represent the magnitude of the currents. Permanent magnets are indicated by the orange rectangles.

An idealized diagram of the voltages through a DC ion thruster is given in Fig. 4. The beam voltage, V_B , determines the ion velocity and is the potential of the engine body relative to the ambient space plasma. The screen grid power supply provides the voltage V_S , and the accelerator grid power supply provides V_A . Neutralizer common shown in this figure represents the physical wire attached to the body of the neutralizer hollow cathode. The ambient space plasma potential is indicated by the line marked $V = 0$. The neutralizer coupling voltage, V_C , is defined as the potential difference between neutralizer common and the ambient space plasma (or facility ground when testing in ground-based vacuum chambers). The beam voltage is calculated by subtracting the coupling voltage, V_C , from the applied high voltage, V_S ,

$$V_B = V_S - V_C \quad (1)$$

The neutralizer coupling voltage adjusts automatically so that the correct electron current is drawn from the neutralizer cathode into the ion beam. If too few electrons are drawn from the neutralizer, neutralizer common becomes more negative by virtue of the excess electrons left behind. The resulting increased voltage difference between the neutralizer and the ion beam increases the electron current drawn into the beam restoring the balance between the ion and electron currents. If too many electrons are drawn, the magnitude of the neutralizer coupling voltage decreases, causing a decrease in the electron current and again restoring the necessary current balance.

The total voltage, V_T , is the sum of V_S and V_A , i.e.,

$$V_T = V_S + V_A \quad (2)$$



The discharge voltage, V_D , is supplied by the anode power supply and serves to maintain the discharge chamber hollow cathode approximately 25 V negative of the anode-potential walls.

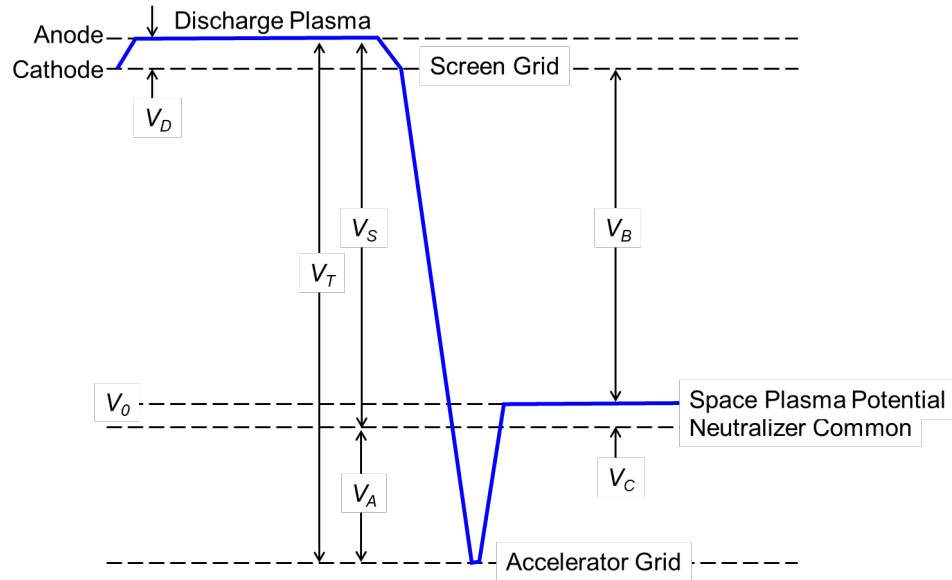


Figure 4. Idealized potential variation through a DC ion thruster.

Demonstrating that the performance and life of a gridded ion engine meets the mission requirements is a critical part of the engine's flight qualification. To characterize the performance requires measurements that may be unique to the particular engine type. Key performance parameters include: the ion optics performance; neutralizer cathode margin; discharge performance; thrust vector location and change with throttle level. Understanding the effects that the test facility background pressure and plasma have on assessing true engine performance is critical. In this work, we review these measurement parameters and in particular, discuss standard characterization methods. The motivation for these approaches is discussed with the goal of standardizing measurements, but in an approach that captures the salient physics. This latter point is critical in that it allows data to be transportable and allows for more or less direct comparison with or assessment of documented engine test data in the published literature. Such considerations are critical for modeling as well for model validation traceability. Another key goal of this work is to provide guidance for new practitioners. In this way, the knowledge based is passed down to the next generation of ion thruster researchers. Each engine type has its own peculiarities regarding characterization of the engine performance and life. An objective of this document is to describe how engine performance and life characterization is best achieved along with how to obtain the data needed for integration of a gridded ion propulsion subsystem with a spacecraft.

II. DC Ion Engines Arcing and Recycling

A key consideration in the operation of an engine is managing potential arcing events which can occur between the high voltage grids. Grid surface imperfections such as localized asperities, rough surface texture or a nonuniform gap (too close in areas) can lead to cathode spot formation and ultimately arcing which can lead to grid damage. Typically, field emission locally initiates the discharge which then can transition into a localized cathode spot. A cathode spot is essentially a vacuum arc fueled by molten grid material locally. Small arc events are typically



observed on start up where they essentially “clean up” small asperities from the electrode surfaces.. This process is known as conditioning and is typical of any set of high voltage electrodes which typically leads to higher voltage standoff. Such cleanups events abate over time. Here the protrusions burn off the asperity, generally leaving a smoother surface. Larger events, however, are more problematic. The energy driven through all arc events must be controlled to prevent significant damage. As part of the set up some form of protection is needed, usually in the form of arc detect and arrest circuitry. Arc protection circuitry is often used in both ground test and flight hardware to manage electrical discharge events within gridded ion thrusters. A multi-step process, sometimes referred to as a “recycle” within the literature, involves the rapid detection of an over-current condition and the subsequent extinguishing of the arc by disabling and then re-enabling the high-voltage supplies. To prevent electron back-streaming, the accelerator grid voltage is re-enabled prior to the beam (screen) voltage. During this sequence, the discharge current is typically reduced to a “cutback” level to minimize plasma loading on the accelerator grid and reduce the likelihood of sustained recycling events. Effective circuit design requires rapid fault detection, energy-limiting mechanisms, and robust integration with the PPU to safely disable and restore grid voltages. A detailed treatment of circuit design is beyond the scope of this paper; readers are referred for discussions on design considerations, transient plasma calculations, arc types and suppression methods, and relevant material investigations. In any case, if the arc event is not managed, the grids are in danger of being destroyed¹⁻⁶.

III.Calculated Thrust with Beam Divergence & Charge State Measurements

Once the thruster is running, key parameters of interest include thrust and beam divergence. The latter gives insight into whether the plume will interfere with structures and whether thrust optimized. Plasma plume measurements, in combination with thruster telemetry, offer an indirect but effective method for estimating thrust in gridded ion engines. This method has been shown to yield results in close agreement with direct thrust stand measurements⁷. This approach involves measuring the spatial distribution of ion current density, as well as identifying the charge state composition of the beam. Faraday probes are typically used to acquire current density profiles, while instruments such as ExB probes are used to resolve charge states. Noting that the total ion current may be expressed by the beam current J_b , and assuming that the ions are monoenergetic, the thrust can be expressed by the simple relation⁸:

$$T = \eta_d \eta_s J_b \sqrt{\frac{2 m V_b}{q}} \quad (3)$$

where m/q is the mass to charge ratio, V_b is the beam voltage, and η_d and η_s are thrust correction factors. The thrust correction factor for beam divergence, η_d , can be estimated from measured current data by taking the ratio of the axial component of beam current, J_{axial} , to the total beam current:

$$\eta_d = \frac{J_{axial}}{J_b} = \frac{\int_A j_b(r) \cos(\theta) (r) dA}{\int_A j_b(r) dA} \quad (4)$$

where j_b is the current density, θ is the polar angle measured from the thrust axis, and r is the position vector. Far-field probe measurements are commonly used to estimate plume divergence assuming spherical expansion from a point source. This assumption, however, may require validation through additional analysis or complementary probe diagnostics^{9,10}. Facility background pressure can also lead to error in accessing beam thrust and divergence.

The general thrust correction factor for multiply charged ions, η_s , can be calculated from:

$$\eta_s = \frac{1 + \sum_{i=2}^N \frac{1}{\sqrt{i}} f_i}{1 + \sum_{i=2}^N f_i} , \quad f_i \equiv \frac{J_i}{J_1} \quad (5)$$

where f_i is the current fraction of charge state i . This parameter takes into account the fact that thrust produced by the acceleration for example of a doubly charged ion is less than that of acceleration to two ions. Sections IV and V



provide further detail on the acquisition of beam current density profiles and ion charge state, including measurement considerations and illustrative examples.

IV. Beam Current Density Profiles

Beam current density measurements are an important diagnostic for the characterization and design of gridded ion thrusters. These measurements provide information on beam uniformity, symmetry, and plume divergence, and can reveal issues such as grid misalignment, localized erosion, or non-ideal plasma conditions that can degrade thruster performance and reduce operational lifetime. Current density profiles may be obtained during thruster development and qualification efforts to validate assembly procedures and confirm proper ion optics alignment. These data can also be used as an aid for determining operational parameters, such as screen and accelerator voltages, and evaluating the impact of design variables such as magnetic field topology, grid spacing, and aperture geometry¹¹⁻¹⁵. Additionally, experimental current density data serve as inputs for modeling grid erosion, roll torque, and spacecraft-plume interactions¹⁶⁻²⁰. The following subsections outline considerations for obtaining near- and far-field probe measurements and present key performance metrics.

A. Near-field Measurements

Near-field current density measurements reported within the literature are typically obtained along the thruster centerline, at axial distances several centimeters downstream of the thruster exit plane, using an electrostatic probe biased to operate in the ion saturation regime²¹⁻²⁵. Measurements acquired within millimeters of the thruster exit plane can resolve the structure of individual beamlets, whereas beam profile measurements are obtained at distances sufficient for the ion beamlets to coalesce into a continuous plume. Considerations such as probe design, thermal loading, and test facility geometry play a role in defining the optimal measurement location. Faraday probes, along with their variants (e.g. Faraday cups), are standard diagnostics for measuring ion current density. Several factors should be accounted for when acquiring near-field current density measurements in gridded ion thrusters:

- a) Ancillary diagnostics or modeling should be used to characterize local plasma properties to define the appropriate ion saturation regime for probe operation. The probe collector diameter should be selected based on the expected range of ion current density and the desired spatial resolution. While there is no standardized value for the degree of ion saturation in the near-field environment, probe bias potentials between -20 V and -80 V relative to facility ground have been reported in the literature.
- b) Probe-related effects must be properly addressed during data analysis to ensure accurate current density measurements. Secondary electron emission, sheath expansion, and the collection of CEX ions may affect the measured probe current, leading to errors if the physical probe area is used. These effects can largely be mitigated through proper probe design. Methods to estimate the effective probe area include modeling²⁶ and adjusting the probe area such that the integrated current density equals the beam current.
- c) Off-axis ion collection should also be considered, as it can affect the measured current density profile. Mitigation approaches include applying angle-of-incidence correction factors, using collimated probe designs, or careful selection of the probe sweep path. For flat grid geometries, radial sweeps perpendicular to the grid surface are preferred, while for convex grids, a polar stage aligned with the grid curvature enables the probe to remain approximately normal to the local ion flow direction. This configuration helps minimize angular misalignment and improves the accuracy of measurements, particularly at large radial positions where oblique ion incidence can affect probe signals.

For further guidance, the reader is referred to Ref. 27, which provides detailed information on Faraday probe design, implementation considerations, and data analysis procedures for both near- and far-field measurements. Sample near-field beam profiles are shown in Fig. 5 for different gridded ion engine designs.



The 39th International Electric Propulsion Conference, Imperial College London,
London, United Kingdom 14-19 September 2025

Page 9

Copyright 2025 by the Electric Rocket Propulsion Society. All rights reserved.

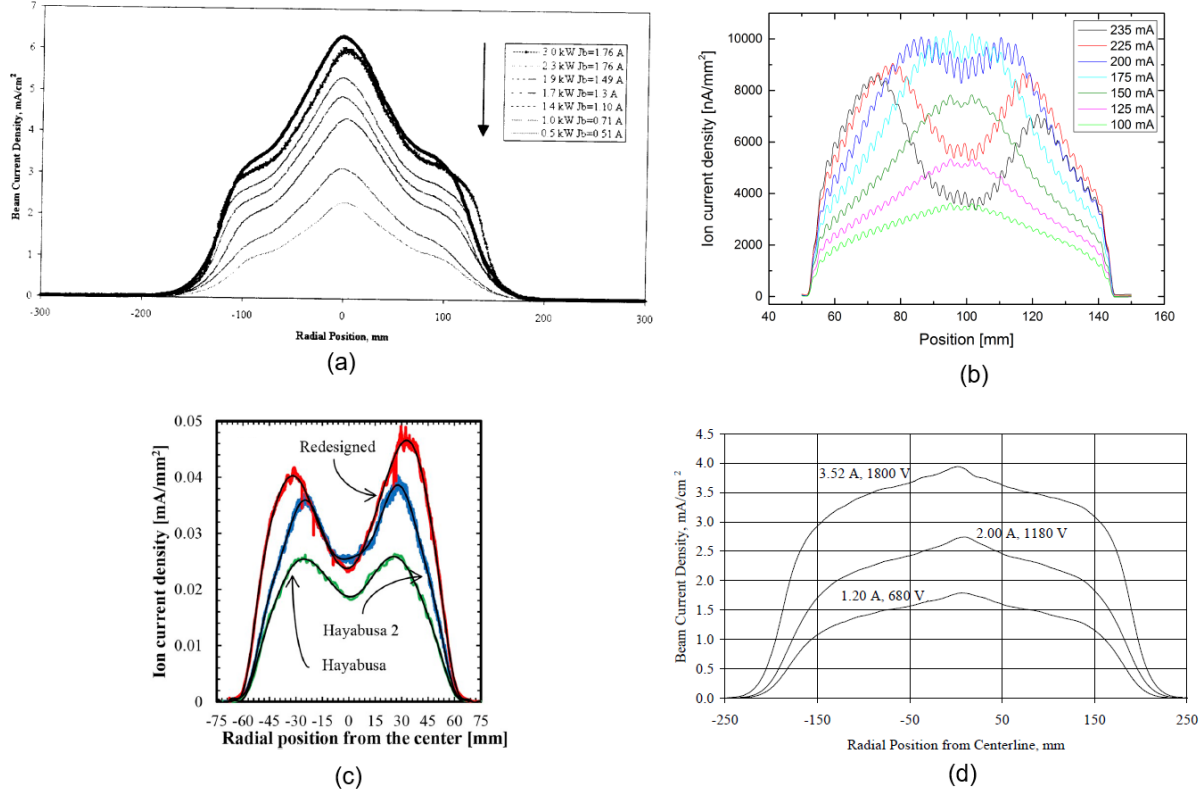


Figure 4: Near-field current density profiles for the a) NSTAR²¹, b) RIT-10²², c) μ 10²³, and d) NEXT²⁴ ion thrusters. The traces were obtained on-centerline, at distances of 30–50 mm downstream of the thruster.

A key metric derived from near-field measurements is the flatness parameter, f_p , which quantifies the spatial uniformity of ion current density across the beam profile. It is defined as the ratio of the average to the peak current density:

$$f_p = \frac{\int_0^{R_g} 2\pi r j_b(r) dr}{\pi R_g^2 j_{b,max}} \quad (6)$$

where r is the radial probe coordinate and, R_g is the grid radius. A higher flatness parameter is desired, as it correlates with improved electrostatic performance of the engine. Additionally, a flatter beam reduces localized accelerator aperture erosion, extending the operational lifetime of the accelerator grid²⁸.

While near-field beam current density measurements are typically reported along the thruster centerline, two-dimensional mapping across multiple vertical planes may be necessary to resolve off-axis features that influence thruster performance. For instance, 2D near-field measurements reported in Refs. 29 and 30 identified a highly localized off-axis current density concentration that caused direct ion impingement on the ion optics, limiting operation at high beam current conditions. Figure 5 shows a 2D contour plot obtained 30 mm axially downstream of the thruster exit plane highlighting the off-axis concentration. Modifications to the discharge chamber were made to eliminate the current density concentration, which yielded a substantial improvement in perveance margin and enabled operation at the desired throttle levels. Thrust vector probes to be discussed later also provide insight into plasma discharge uniformity and grid misalignment and drift over time.

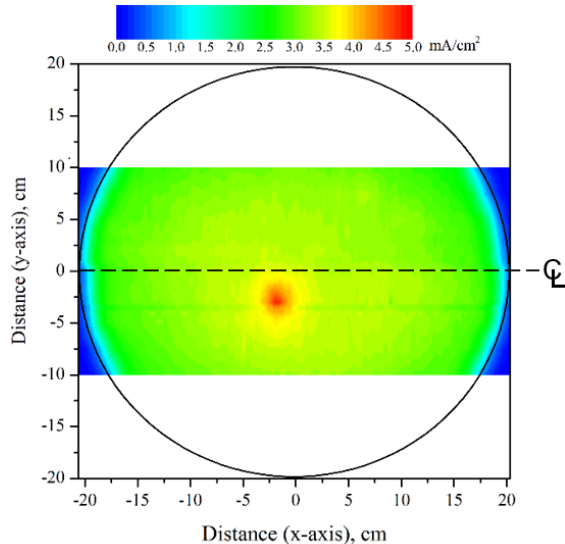


Figure 5. Near-field 2D current density map illustrating an off-axis current density concentration.

B. Far-field Measurements

Far-field measurements provide information on plume behavior, including beam divergence, thrust vector offsets, and parameters required for modeling plasma-spacecraft interactions. A key consideration in acquiring these measurements is the selection of an appropriate probe standoff distance from the thruster. The distance required for accurate far-field measurements is primarily determined by the thruster geometry, beam dynamics, and the desired resolution. Increased probe distances improve the angular resolution and enable more precise evaluation of plume symmetry. Published guidelines recommend probe placements at downstream distances of at least eight thruster radii to effectively capture the expansion characteristics of the plume^{27,31}. Ultimately, practical limitations such as vacuum chamber dimensions and acceptable background pressure levels may restrict the achievable range of probe positions.

Figure 6 illustrates a hemispherical coordinate system that has been utilized in far-field probe measurements for the qualification testing of gridded ion thrusters. This configuration has been applied in tests using a single probe swept along the thruster centerline³², as well as with multi-probe arrays used to generate two- and three-dimensional maps of the beam current density³³⁻³⁵.

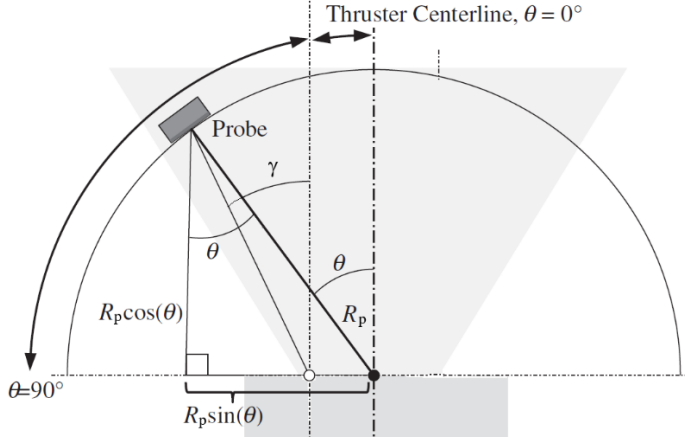


Figure 6. Hemispherical coordinate system for far-field probe measurements²⁶.

Using this coordinate system, Eqn. (Error! Bookmark not defined.) takes the form:

$$\eta_s = \frac{J_{Axial}}{J_b} = \frac{\int_{\theta_1}^{\theta_2} \kappa j_b(\theta) \cos(\gamma) \sin(\theta) d\theta}{\int_{\theta_1}^{\theta_2} \kappa j_b(\theta) \sin(\theta) d\theta} \quad (7)$$

where κ is a correction factor that accounts for the ion angle of incidence and the axial distance between the probe and the thruster, and the angle γ is described below. The divergence angle (λ) may be calculated using:

$$\lambda = \cos^{-1} \left(\frac{J_{Axial}}{J_b} \right) \quad (8)$$

Several considerations must be addressed when acquiring far-field plume measurements. To account for errors associated with the assumption of spherical plume expansion from a single point source, the angle γ is introduced in Eqn.5. The reference location associated with this angle depends on the ion beam behavior and the trajectory of ions as they exit the thruster. As an example, Pollard et al., in experiments conducted with the NEXT engine³⁶, observed that the grid-normal coordinate system does not accurately represent ion trajectories beyond the angular extent of the convex grid geometry. As a result, γ was defined as a multi-valued function. Within the angular extent of the optics, $\gamma = \theta$; beyond this region, γ was defined by the angle formed between the probe position and the outer edge of the ion optics, providing a more accurate basis for evaluating beam divergence at large radial distances.

The presence of scattered or CEX ions necessitates careful selection of integration limits to avoid disproportionately weighting these low-energy ion populations in the analysis. Various methods exist to minimize the influence of non-beam ions, including the use of energy-selective diagnostics and appropriate data processing techniques such as curve fitting. In a study by Young et al.³⁷, current density measurements were obtained at axial distances up to 2.8 meters (14 thruster radii) downstream of the engine using both a planar Faraday probe and a retarding potential analyzer (RPA) biased to exclude CEX ions. Due to its narrower field of view and ability to discriminate based on ion energy, the RPA was found to more effectively isolate the beam ions, leading the authors to conclude that it was the preferred diagnostic for far-field plume characterization. Similarly, researchers³³ often utilize collimated probes to mitigate errors associated with the collection of off-axis ion current during measurements.

Curve fitting can be used for separating the contributions of primary beam ions and CEX ions in the far-field plume region. The measured ion current profile contains a high-density central region corresponding to the primary beam and broad, low-intensity wings resulting from CEX ions produced through interactions with residual background gas. By fitting the measured data to a composite function, typically a Gaussian to model the core beam and an exponential or power-law function to represent the CEX population, it is possible to analytically distinguish between the two components and use extrapolation to define the integration limits. Curve fitting examples are shown in Fig. 7 for two different engine designs.



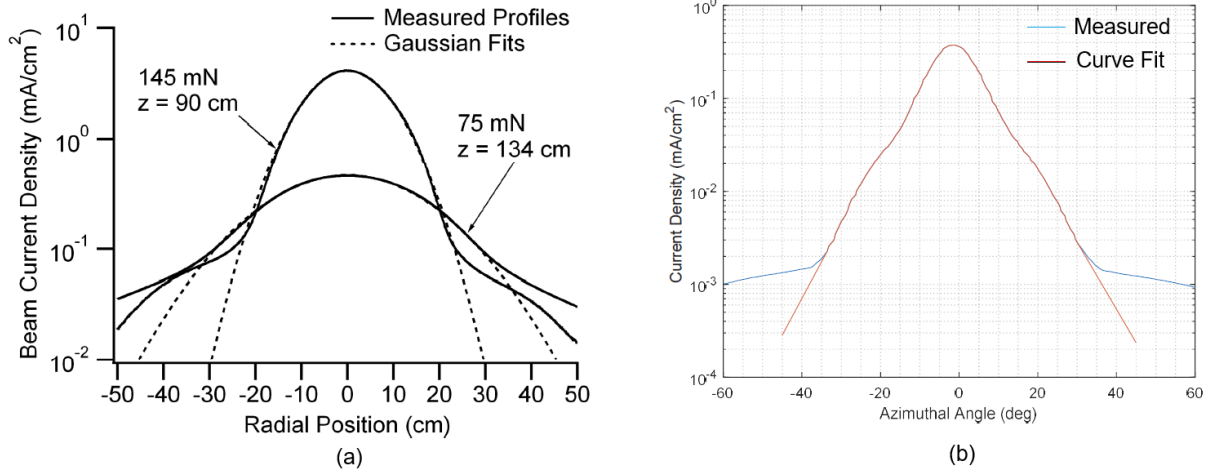


Figure 7. Measured beam profiles and their associated curve fits for the a) T6³⁸ and b) NEXT-C³² ion thrusters.

The measurement configuration illustrated in Fig. 6, which utilizes a far-field probe swept azimuthally across the full extent of the thruster plume, offers wide angular resolution and insight into plume symmetry. However, this approach is not always practical due to spatial and geometric constraints of available test facilities. Alternative methods have been developed and demonstrated successfully. For instance, researchers in Refs. 38 and 39 performed radial sweeps at various axial positions to reconstruct the beam profile and determine plume divergence. When utilizing this method, it is common to report the beam divergence as the half-cone angle that contains 95% of the total ion current, which is determined by integrating the measured current density distribution and identifying the angle at which this threshold is met.

V. Multiply-charged Ion Content

Charge state measurements play an important role in understanding the physical processes occurring within the discharge chamber and in evaluating overall thruster performance. Although most of the thrust is generated by singly charged ions, the presence of multiply charged ions can degrade propulsive efficiency and contribute to accelerated erosion of the ion optics. Determining the relative abundance of each charge state provides insight into ionization dynamics within the discharge chamber and enables assessment of how different operating conditions (e.g. discharge voltage, propellant utilization) may influence the production of higher charge states. These measurements are also required for calculating thrust correction factors and validating numerical models.

Different plasma diagnostics can be used to infer charge state distributions, including ExB probes^{23, 36, 38, 40-42}, time-of-flight spectrometers⁴³, and magnetic sector mass spectrometers⁴⁴. Amongst these, ExB probes have found widespread adoption within the electric propulsion community due to their compact form factor, operational simplicity, and cost-effective capability to resolve ion charge states. Additionally, the narrow energy spread characteristic of gridded ion thruster beams simplifies the interpretation of data. For detailed guidance on the application of ExB probes in electric propulsion plumes, the reader is referred to Ref. 45, which outlines best practices related to design, probe alignment, data analysis methodologies, and accounting for facility effects.

As noted earlier, one of the principal quantities obtained from charge state measurements is the thrust correction factor, η_s , which accounts for the presence of multiply charged ions. Accurate determination of η_s requires measurement of the radial distribution of multiply charged ions across the ion beam. These spatially resolved data enables integration over the beam cross-section to account for local variations in charge state. Measurements should be acquired with sufficient spatial resolution to capture the relevant characteristics (e.g. asymmetric behaviour) of the beam profile. It is common to supplement the charge state measurements with beam profile measurements to determine



the total current fraction associated with each charge state. Utilizing the coordinate system defined in Fig. 6 and neglecting the typically minor contribution from triply charged ions, the total current ratio can be expressed as:

$$\frac{J^{++}}{J^+} = \frac{\int_{\theta_1}^{\theta_2} \frac{f_2}{1+f_2} j_b(\theta) \sin(\theta) d\theta}{\int_{\theta_1}^{\theta_2} \frac{1}{1+f_2} j_b(\theta) \sin(\theta) d\theta}; \quad f_2 = \frac{j^{++}}{j^+} \quad (9)$$

The total current fraction can be used to calculate the charge state correction factor, which for doubly charged ions reduces to:

$$\eta_s = \frac{1 + \frac{1}{\sqrt{2}} \frac{J^{++}}{J^+}}{1 + \frac{J^{++}}{J^+}} \quad (10)$$

VI. Ion Optics Measurements

The following section will review typical optics performance measurements needed to characterize engine performance. These measurements include accelerator and decelerator currents, perveance limits, electron backstreaming limits, beam divergence, and thrust vector. The latter two measurements are plume measurements that are largely impacted by the optics design and are therefore categorized as optics measurements in this standard.

A. Accelerator and Decelerator Current Measurements

Accelerator current referred to here is the ion current collected by the accelerator grid during beam extraction (i.e. thrust generation). The magnitude of this current is significant for two reasons: 1) it impacts the total thruster input power; and 2) it impacts the service life capability of the accelerator grid. Accelerator current is typically dominated by charge-exchange ions created with propellant neutrals and beam ions. Direct beam ion impingement of the grid is typically minimized to maximize accelerator grid service life. These charge exchange ions are created in the inter-grid region and downstream of the accelerator grid and typically impact the accelerator aperture barrel walls and downstream surface⁴⁶. Because accelerator current is dominated by charge exchange ions created downstream of the discharge chamber, this current is sensitive to vacuum chamber background pressure, with higher pressures causing larger currents⁴⁷.

Accelerator current is a power loss mechanism that is processed by the accelerator and beam power supplies. However, accelerator currents are typically < 1% of the ion beam current. For example, accelerator currents of the NEXT and NSTAR thrusters during ground tests were < 0.4% of the beam current⁴⁸⁻⁵⁰. As a result, these powers typically represent an insignificant fraction of total thruster input power.

Regardless, accelerator current should be measured to assess its impact on thruster input power for performance assessments. While a direct current measurement with a digital multimeter is typically more accurate, a grid arc that leads to a recycle can trip the multimeter's overcurrent protection. Measuring the voltage across a current shunt is recommended. Additionally, accelerator current measurements used for performance assessments should be made at the lowest background pressures achievable due to current sensitivities with background pressure.

Some ion thrusters utilize a third decelerator electrode downstream of the accelerator grid. This grid is typically held near ground potential. It has essentially 3 functions: 1) It enables operation at low specific impulse and high extracted ion current (without the third grid, the resulting beam is very divergent). The third grid facilitates focusing. 2) It shields the accel grid from CEX erosion by minimizing the potential difference between CEX ions and the grid and 3) It shields the accel grid from backspattered material.



B. Perveance and Cross-over Impingement Limits

A given grid set geometry ion throughput is limited by geometry regardless of the applied voltage. An understanding of the operational limits of grids is key to characterizing engine performance and limitations of a given grid set. Ion grids impingement limits represent the range of beam voltage and extracted ion current that a given ion optics set can safely deliver. These impingement limits are due to beam ions being deflected into the accelerator grid (and decelerator grid for three grid systems). An example is shown in Fig. 8. There are two impingement limits. The commonly reported limit is the under-focusing limit that occurs at lower grid voltages, where beamlet ions are defocused into the downstream grids. This is commonly referred to as the impingement-limited perveance. The less common is the over-focusing limit that occurs at high grid voltages, where beamlet ions are over-focused leading to impingement into the downstream grids. At both limits, further voltage decreases at the under-focused limit or increases at the over-focused limit can lead to dramatic increases in impacted grid currents. Operation at or beyond these limits is not feasible due to rapid grid sputter erosion, as well as increased power losses. Plots of accelerator current as a function of grid voltage typically can also show gradual accelerator current changes with voltage prior to the impingement limit. This can be due to several causes, such as aperture misalignment and variations in grid gaps, aperture diameters, and beamlet currents throughout the grid, though there can be other causes. In any case, the perveance curve should be considered a critical measurement in assessing engine performance and life.

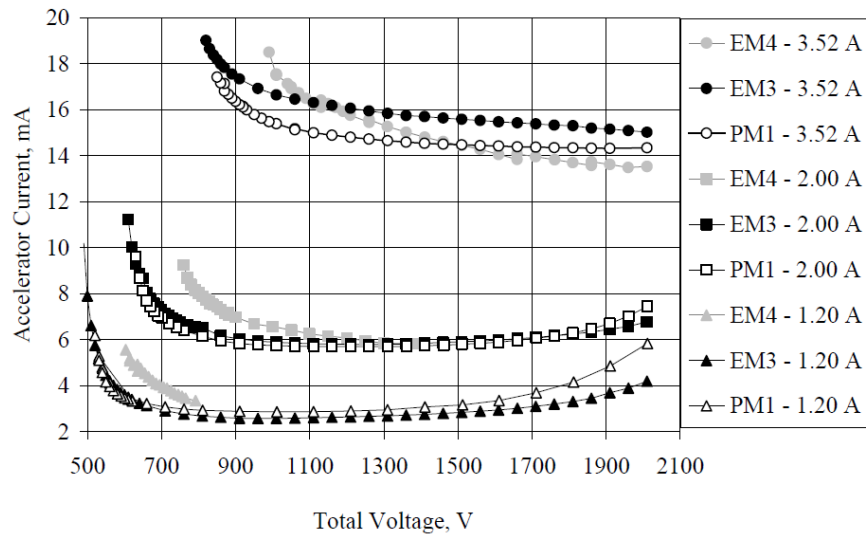


Figure 8. Impingement limits for the NEXT thruster⁴⁸.

Each impingement limit is typically measured by adjusting the beam power supply voltage, though the accelerator power supply voltage can also be adjusted during operation at low R-ratios. If the accelerator voltage is adjusted, however, care should be taken to avoid electron backstreaming during under-focusing measurements. For decreasing grid voltages, the beam current decreases as the sheath meniscus at the screen apertures retracts. The opposite occurs as grid voltages are increased. The discharge power can be adjusted to compensate for these effects to maintain a constant beam current. For the NSTAR and NEXT programs, for example, discharge current was adjusted to maintain a constant beam current during impingement-limited perveance limit measurements⁴⁸⁻⁵⁰. Discharge propellant flow can also be used to maintain beam current, however, the resulting changes in discharge propellant utilization efficiency can impact accelerator currents from charge-exchange, potentially obfuscating results. At least one past study maintained fixed discharge input parameters and noted the beam current when the impingement limit was reached⁵¹. Impingement limit measurements can sometimes induce arcing, generating one or more recycle events. Care should be taken evaluating such measurements because the recycle event can lead to sudden shifts in accelerator current, obfuscating the limit measurement.



The definition of the “impingement limit” can vary from study to study. For example, the NSTAR and NEXT programs defined the underfocusing limit as a slope of -0.02 mA/V for the under-focusing limit^{48,50}. Other studies have used a fixed increase in the ratio of accelerator-to-beam current⁵². Whatever method is used, it is more important to present the plotted results and include the limit definition.

The reported grid voltage is also a consideration. For a DC discharge with the beam power supply electrically connected to the discharge anode, the voltage between the grids is beam power supply voltage plus the accelerator voltage magnitude minus the discharge voltage because the screen grid is typically tied discharge cathode. However, the discharge plasma typically resides at a potential above the anode potential. So, in this instance, the reported total voltage is commonly taken as the sum of the beam power supply voltage plus the accelerator voltage magnitude. When the beam power supply is electrically tied to screen grid, the discharge voltage is further added to this.

Along with the optics aperture diameters, thicknesses, and alignment, impingement limits are sensitive to grid gaps, discharge voltages, and peak beamlet currents. Measurement procedures should consider these effects and configurations reported if any reasonable comparison with literature is to be made.

C. Electron Backstreaming Limit

Because the applied accelerator voltage functions to focuses beam ions and provides energy to charge-exchange ions for accelerator grid sputter erosion, a low accelerator voltage magnitude is typically beneficial during operation at high R-ratios. This accelerator voltage creates a potential well that acts as a barrier for neutralizer electrons from backstreaming into the discharge chamber. The lower limit of this barrier is referred to as the electron backstreaming limit. At this voltage and at voltage values less negative electrons can enter the grid gap and be accelerated to essentially the total voltage leading to damage of discharge structures including the discharge cathode.

The electron backstreaming limit has been measured using a couple of methods. For fixed discharge input conditions (i.e. no beam current regulation), the electron backstreaming limit is typically measured by lowering the magnitude of the accelerator voltage while monitoring the beam current. As this voltage magnitude is lowered, the beam current decreases gradually due to changes in the screen sheath meniscus (i.e. screen grid ion transparency decreases). However, as the backstreaming limit is approached, neutralizer electrons can overcome the potential barrier and backstream through the optics apertures into the discharge, and are included as beam current. This effect rapidly overcomes the decreasing screen grid ion transparency and results in an increasing beam current. A fixed increase in beam current is commonly used to define this limit. For example, the NEXT program used a beam current increase of 1 mA to define this limit⁵⁰.

Another technique to determine the electron backstreaming limit involves measuring discharge losses during regulated beam current operation. This technique was used during much of NSTAR wear testing⁵³. As the accelerator voltage magnitude is lowered and energetic neutralizer electrons begin to backstream through the optics, the resulting discharge power required to maintain the beam current decreases during regulated beam current operation. For the NSTAR wear tests, a discharge losses decrease of 1% was used to define the electron backstreaming limit.

Along with the optics accelerator grid aperture diameter and thickness, electron backstreaming limit is sensitive to the grid gap⁵⁴. For large area, domed optics, this gap is typically sensitive to thermally-induced changes due to uneven grid heating^{55, 56}. Electron backstreaming limit measurement procedures should account for this effect (for example, avoid steady state measurements during thermal transients). The electron backstreaming limit can also be impacted by peak beam current densities and neutralizer operation^{47, 54}. Electron backstreaming limit measurement procedures should also consider these effects.

VII. Discharge Losses

The efficiency of the ionization stage on any ion engine is a critical factor that contributes to the efficiency and performance of a gridded ion engine. The ionizer stage performance metric is often called discharge losses. It refers to the power that is required to be deposited into the discharge plasma to realize a given beam current. This power accounts for inelastic processes such as excitation and ionization as well as both ion and electron losses to the wall



and gas phase thermalization processes. Discharge losses are a function of ionization method, discharge chamber magnetic field topology, discharge chamber geometry and grid geometry which determines neutral density. Larger grid apertures lead to a greater loss rate of neutral propellant gas which in turn increases the power required to attain the desired beam current. Similarly, longer discharge chamber can increase wall collisions and recombination of ions which contributes to an increase in the discharge loss.

The basic equation to calculate the discharge loss, η_d , is given in Eq. 11 below,

$$\eta_d = \frac{\text{Discharge Power}}{\text{Extracted Ion Current}} = \frac{P_{\text{Discharge}}}{I_b} \quad (11)$$

Here the I_b is the beam current in ampere. The unit of discharge loss is watts per ampere (W/A) or electron-volts per ion (eV/ion). The beam power supply is usually configured electrically to the discharge chamber anode. When this is the case, the discharge loss is calculated as,

$$\eta_d = \frac{P_{\text{Discharge}}}{I_b} = \frac{V_d * I_d}{I_{b,\text{true}}} \quad (12)$$

Here V_d is the discharge voltage which must be measured with high voltage differential probe. I_d is the discharge current determined by measuring the current on the cathode line and subtracting the discharge keeper current one is actively being used. The beam current is measured from the neutralizer common line illustrated in Fig. 3. It is also the difference between the current of the anode line minus the accel current.

The discharge loss is given by:

$$\eta_d = \frac{(V_{\text{anode}} - V_{\text{cathode}}) * (I_{\text{cathode}} - I_{\text{discharge keeper}})}{I_{\text{anode}} - (I_{\text{cathode}} - I_{\text{discharge keeper}}) - I_{\text{accel}}} \quad (13)$$

When the beam power supply is electrically connected to the cathode, the beam power supply references the cathode potential. The discharge loss is then calculated as,

$$\eta_d = \frac{(V_{\text{anode wrt cathode}}) * (I_{\text{anode}})}{I_{\text{anode}} + I_{\text{discharge keeper}} - I_{\text{cathode}} - I_{\text{accel}}} \quad (14)$$

Here the discharge voltage can be measured using a differential probe between the anode and the cathode.

A. Propellant Utilization

The optimal operating condition for the discharge may be determined by plotting the discharge losses as a function of propellant utilization—a measure of the fraction of ions that reach the extraction plane of the engine⁵⁷. Too high of a utilization translates into high discharge losses as power is lost due to inelastic processes that don't produce singly charge ions such as excitation and doubly charge ions. Under such conditions this waste power increases is reflected in high discharge losses. Low utilization implies an inefficient ionizer which translates into higher discharge power to maintain the desired beam. These trends imply an optimum condition where the discharge losses are low and the utilization is reasonably high. Propellant utilization, η_u , is calculated as the ratio of mass flow rate of ionized propellant, \dot{m}_i , to total mass flow rate of propellant, \dot{m}_t , fed into the discharge chamber as given in Eq. 15.

$$\eta_u = \frac{\dot{m}_i}{\dot{m}_t} \quad (15)$$

The total mass flow rate of propellant fed into the discharge chamber includes the main plenum flow, discharge cathode flow and any neutral gas ingested back into the discharge chamber. The mass flow rate of ionized propellant can be expressed using the beam current, I_b , as



$$\dot{m}_t = \frac{I_b * M}{q} \quad (16)$$

Here the M is the atomic mass of the propellant in kg/ion and the q is the elementary charge of an electron (assuming singly charged ions):

$$\eta_u = \frac{I_b * M}{q * \dot{m}_t} \quad (17)$$

Measurements of discharge losses are made while varying the propellant utilization. The propellant utilization is varied by adjusting the main flow to the discharge cathode flow ratio while keeping the discharge voltage and beam current constant. It is observed that an increase in propellant utilization increases the discharge losses. Figure 9 shows the discharge losses as a function of the propellant utilization that was measured during the NASA's Evolutionary Xenon Thruster (NEXT) Long-Duration Test (LDT) for full-power and low-power conditions⁵⁸.

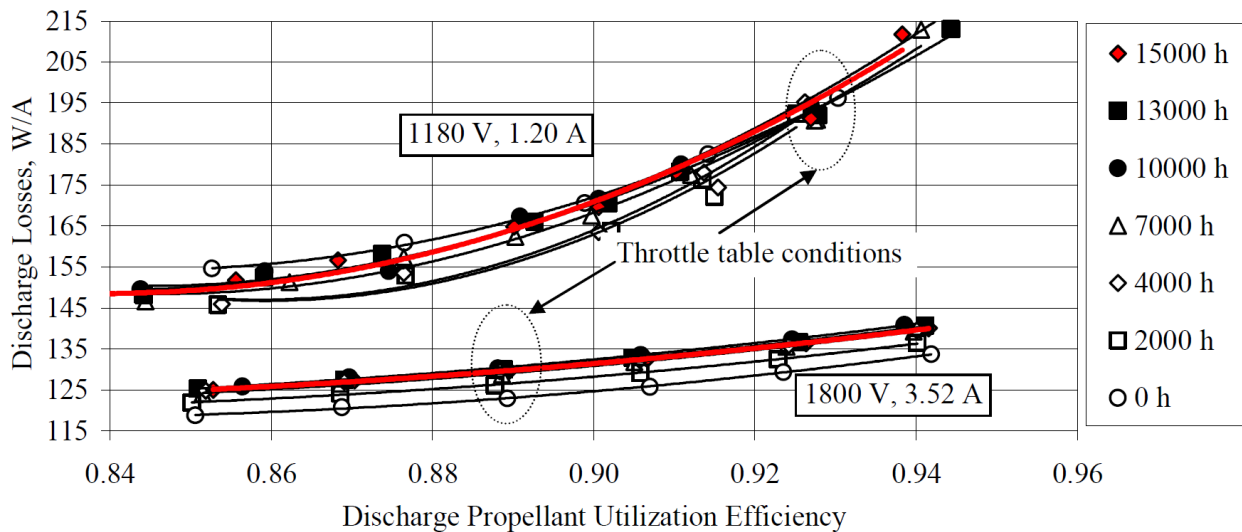


Figure 9. Discharge losses as a function of discharge propellant utilization efficiency (including mass ingested) for full-power and low-power conditions after various test durations with fixed discharge voltages of $23.5 \text{ V} \pm 0.5 \text{ V}$ and $26.0 \text{ V} \pm 0.5 \text{ V}$, respectively.

As shown in the figure, high utilization is usually undesirable owing to inelastic collisions which do not produce singly charged ions to maintain a fixed beam current⁵⁹. As mentioned earlier, very low utilization also leads to high discharge losses since increased discharge power again is required to maintain the desired beam current and minimize escaping neutrals, which lead to increased charge exchange.

The optimum operating condition is located at the knee in the curve where balance is struck between high propellant utilization (high thruster efficiency) and low discharge losses (minimum fuel consumption). Any further increase in the propellant utilization drastically increases the discharge losses and any further decrease in the propellant utilization only improves the discharge losses slightly. For example, the NEXT operates between 0.88 and 0.93 propellant utilization.



VIII.Thrust Vector probe

The ion optics for gridded ion thrusters consist of two or more closely spaced, multi-aperture electrodes. A mechanical fixture is used to align the grid apertures, maintain this alignment under thermal and electrostatic loads, and provide the mechanical interface to the rest of the ion thruster. Thermal-mechanical loads produced by thruster operation at different power levels and different thermal environments can change the electrode spacing and aperture alignment. Electrostatic loads due to the applied voltages can also change the electrode spacing. These changes to the effective grid system geometry can change the location of the centroid of the ion beam and the value of the thrust vector.

The changes in the thrust vector must, therefore, be quantified over the full set of throttle settings and environmental conditions that the thruster will see in flight. A means of characterizing the beam centroid is thus an essential diagnostic to complement a single chord Faraday probe sweep. The most straightforward way to watch beam centroid drift in real time as a function of operating condition and operating time is to use a thrust vector probe. Such a probe could be a dense array of Faraday probes imbedded into a target positioned downstream of the thruster. Such a probe system would provide valuable, detailed two-dimensional information about the structure of the ion beam. It would also be complicated to implement such a system and it may not be suitable for long duration ion thruster testing due to damage that the ion beam would do to the Faraday probes.

For this reason, a simpler system is often used, one that is more robust to ion sputtering, but provides less detailed information about the ion beam. In this system, a series of graphite rods are arranged horizontally and vertically and positioned some distance downstream of the thruster. Graphite is used to maximize the sputter-resistance of the rods. The ion current collected by each rod is measured separately providing the integrated current along that particular line. The rods are biased to repel background electrons, typically around -20 V. This voltage also minimizes sputtering by charge-exchange ions in the beam plasma as this value is below the sputter threshold of carbon. By combining horizontal and vertical data, the centroid of the beam can be located as indicated in Fig. 10. The photograph of the system in this figure was used to characterize the T6 and the NSTAR ion engines. This particular thrust vector probe featured a 16 by 16 array of graphite rods measuring 1.2 m in length^{60,61}. An example of data used to extract the centroid is also shown in the figure. These data were obtained using the NSTAR engine⁶². More recently the Next-C engine was characterized using a scaled-up version of this probe as depicted in Fig. 11⁶³. This type of probe design has been used successfully to obtain centroid behavior on second, minute, hour, and khr time scales providing data about thermal and grid wear effects on the thrust vector. For long-durations exposures to the ion beam, erosion of the rods will be non-negligible. The change in shape of the rods must be accounted for in the interpretation of the measured rod currents and the corresponding beam centroid location.

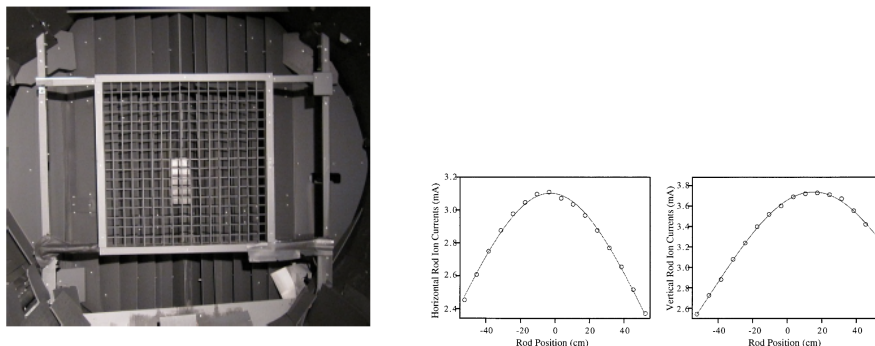


Figure 10. Thrust vector probe used for NSTAR engine and the T-6. Right hand panel shows NSTAR data.



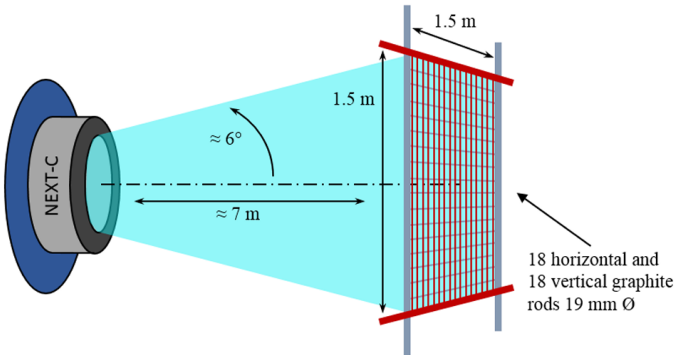


Figure 11. Thrust vector probe lay out scaled up for NEXT-C

IX. Simulated Beam Extraction

The development of high power ion engines may be facilitated using a technique which enables optimization of the discharge chamber to be performed without beam extraction. Early in the development of a new gridded ion thruster, it is often advantageous to test the discharge by itself, i.e., without the application of the high voltages necessary for ion beam extraction. This can be performed in smaller, less expensive-to-operate vacuum chambers and can provide an early assessment of the discharge chamber performance. Ion thruster operation without beam extraction results in a decrease in the accelerator system transparency to ions. This decreased ion transparency translates into a decreased propellant flow rate requirement for operation without beam extraction, enabling testing to be performed in smaller vacuum chambers with lower pumping speeds. Performance curves simulated without beam extraction agree well with actual performance curves obtained with beam extraction. The implementation of this technique for DC ion thrusters is described in Ref. 64.

Discharge chamber performance is strongly dependent on the neutral atom density. In fact, all major discharge chamber plasma parameters are functions of the neutral atom density. To simulate beam extraction, the most important similarity condition is to match both the neutral atom density to the value it would have with beam extraction. With beam extraction, the neutral propellant density in the discharge chamber is typically much greater than the ion density. Yet, in an efficient ion engine, greater than 90% of the propellant leaves the thruster in the form of ions. This is possible because the ions flow toward the accelerator system with a velocity which depends on the electron temperature (i.e. the Bohm velocity), and the electron temperature is generally more than 500 times the neutral atom temperature which governs the escape of neutral atoms from the thruster. In addition, the effective transparency of the accelerator system to ions (67 to 80 percent) is much greater than the effective transparency of the accelerator system to neutral atoms. The neutral atom transparency is governed by the accelerator grid hole size and grid thickness, and is typically around 20%.

Without beam extraction, the situation is different. Removal of the high voltages dramatically reduces the accelerator system transparency to ions. In this case, a large fraction of the ions reaching the accelerator system are focused onto the screen grid and accelerator grids rather than being transmitted through the grid apertures. Ions striking the grids recombine with electrons and leave the surface as neutral atoms. Some fraction of these neutral atoms re-enter the discharge chamber, the rest leave the thruster entirely. Since the accelerator system transparency to ions decreases significantly without beam extraction, the fraction of propellant which leaves the discharge chamber as neutral atoms increases. If the propellant flow rate into the discharge chamber is unchanged when the high voltages are removed, then the neutral atom density in the discharge chamber will increase to satisfy continuity. In this case

the neutral particle flux through the grid must increase to account for the decrease in ion flux from the engine. To simulate the beam extraction operating conditions of the discharge chamber without beam extraction, the propellant flow rate into the discharge chamber must be reduced.

Reference 64 shows that the similarity conditions to simulate discharge chamber performance without beam extraction are that the neutral atom density must be the same with and without beam extraction and the product of the ion density and the square root of the electron temperature must be the same, i.e.,

$$\hat{n}_0 = n_0, \quad \hat{n}_i \sqrt{\hat{T}_e} = n_i \sqrt{T_e} \quad (18)$$

where the “ $\hat{\cdot}$ ” symbol indicates parameters without beam extraction, and n_0 is the neutral atom density, n_i is the ion density, and T_e is the electron temperature. To meet these similarity conditions, the flowrate without beam extraction must be reduced to

$$\hat{m} = \dot{m} \left[1 - \eta_{ud} \left(1 - \frac{\phi_i}{\phi} \right) \right] \quad (19)$$

where \dot{m} is the propellant flow rate, η_{ud} is the discharge propellant efficiency and ϕ is the grid system transparency to ions. This approach was refined and successfully applied to the development of the 65-cm diameter NEXIS ion thruster⁶⁵ and a 50-cm ion thruster⁶⁶.

Finally, screen grid temperatures are significantly higher without beam extraction due to the decrease in the accelerator system transparency to ions. The difference in radial temperature profiles with and without beam extraction are substantial enough that it may be necessary to account for this difference when modeling the thermal mechanical behavior of ion accelerator systems.

X. Microwave Ion Engines and Neutralizers

A. General aspects of microwave system of microwave discharge ion thruster

1. General Microwave Systems and Considerations

A distinguishing feature of microwave-discharge ion thrusters lies in their use of microwave power, as the name suggests. In this section, the term “microwave” primarily refers to electromagnetic waves in the GHz range. Although microwaves are widely used in various devices today, the associated handling and required components differ fundamentally from those of direct current (DC) and low-frequency alternating current (AC) systems, defined here as those below 100 MHz. For researchers who are new to microwave systems, these differences can present a substantial barrier. This section describes the basic configuration and key considerations for generating plasma using microwaves.

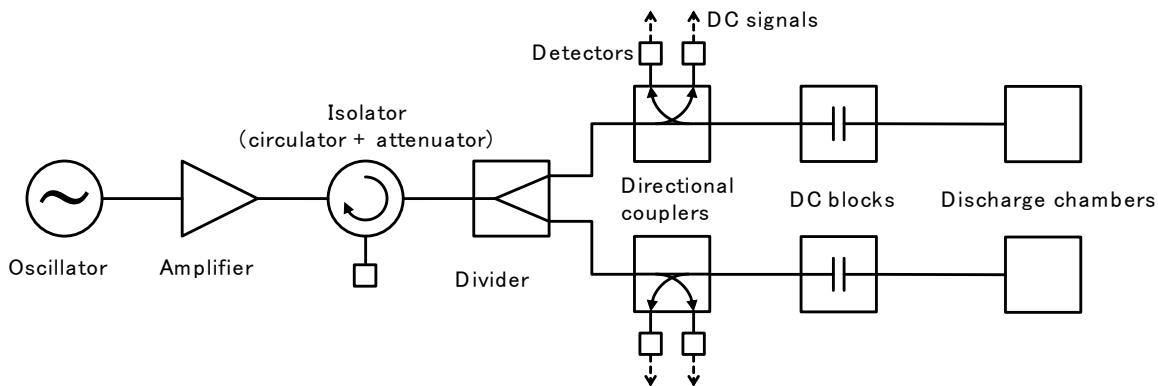


Figure 12. Basic configuration from the microwave power source (microwave generator) to the discharge chambers (plasma generation chambers).



Figure 12 shows the typical configuration from the microwave power source (microwave generator) to the discharge chamber (plasma generation chambers). The core components of the microwave system include an oscillator, an amplifier, and an isolator. Depending on the application, directional couplers, detectors, and power dividers may also be incorporated. These devices are inserted in an order appropriate to the purposes of the experiment (note that this is not necessarily the same as the order shown in Fig.12).

The oscillator determines the frequency of the microwave and may also support frequency or power sweeping. The output power of the oscillator is typically around 1 mW (0 dBm, where dBm denotes decibels referenced to 1 mW), and it is amplified to practical levels (typically 1 to 100 W). The amplification is typically achieved using either a traveling-wave tube amplifier (TWTA), such as those used in the ion thrusters of Hayabusa 1 and 2⁶⁷, or a solid-state power amplifier (SSPA), such as those used in the ion thrusters of Hodoyoshi-4⁶⁸ and PROCYON⁶⁹. TWTAs have a long flight heritage on communications satellites and are suitable for 100 W-class or more output, whereas SSPAs offer compactness and low mass and are commonly used for 10 W-class systems; in recent years, their output capability has also increased. For ground-based testing, magnetrons, a commonly known microwave source used in microwave ovens, are sometimes used in place of the oscillator and amplifier. The isolator plays a protective role by preventing reflected power from reaching the amplifier. The power divider is used when multiple plasma sources need to be fed from the same microwave power supply. The directional couplers extract a small fraction of the microwave power from the transmission line (typically at -10 to -30 dB) by the forward and backward wave, respectively. These extracted microwaves are converted into DC signals using the detectors and are recorded using an oscilloscope or a data logger. Some of these components are available commercially as integrated packages, but they are not always complete, so careful component selection is required when constructing experimental systems. The DC blocks, unique components for biased microwave plasma sources, are explained later in this section and the discharge chambers are described in the following sections in detail.

There are two important considerations when connecting components in a microwave system: first, impedance matching of all components, including cables and connectors, is required; second, even when the characteristic impedances are matched, finite reflections and losses still occur and are not necessarily negligible. The typical impedance is the well-known 50 Ω, and the mismatch can cause significant reflection. The fact that every device and connection point introduces even a small amount of reflection implies that both forward and backward waves undergo infinite successive reflections, continuing until they are sufficiently attenuated. In other words, the forward and backward powers measured at directional couplers are not merely the result of cumulative losses from upstream components, but rather the result of superpositions of all successive reflections in both directions. Although these multiple reflections do not change the microwave frequency, they do alter the phases of the forward and reflected waves. It should be noted that under such conditions, a resonant cavity may form somewhere along the transmission path. Therefore, the intuitive notion that forward power simply decreases downstream and that less reflection is always better is not necessarily valid. Moreover, even a simple change in cable length can result in a significant change in the measured power, although such occurrences are rare.

Actual low power microwave systems require numerous cables to connect components and to place them appropriately. Typically, coaxial cables with matched characteristic impedance are used. It is essential to select cables and connectors with sufficiently low microwave absorption in the intermediate dielectric material, which corresponds to a low imaginary part of the complex permittivity or a low dielectric loss tangent. However, rather than selecting materials directly, it is more practical to choose components based on the specified insertion loss provided for each part or cable. In most cases, semi-rigid coaxial cables with high-stiffness copper outer conductors and PTFE dielectric cores are employed, along with SMA, TNC, or N-type connectors. Flexible cables, such as those with BNC connectors designed for low-frequency signals, should be avoided, as they can result in substantial microwave power loss. Additionally, improper connector torque can cause extra reflection and power loss, making proper torque management essential. Even with appropriate cable selection, transmission losses (e.g., 0.2 dB/m) are inevitable; thus, the transmission line should be kept as short as possible. While greater losses may be tolerable in laboratory settings, microwave sources are typically expensive, and their cost increases rapidly with output power. Therefore, systems should be designed to minimize loss and to operate at the minimum required power within a given budget.

When the power exceeds approximately 100 W, loss due to cable heating becomes non-negligible (it is severe inside the vacuum chamber), and waveguides are instead employed. Waveguides transmit microwaves by utilizing successive reflections within a hollow metallic cavity, which inherently eliminates dielectric losses. Additionally, due



to their operating principle, they must be larger than a wavelength-dependent cutoff size and are made of metal, making them highly heat-resistant. As a result, waveguides are indispensable for high-power microwave transmission. However, waveguides are rarely used unless there are compelling reasons, as they offer extremely limited flexibility in routing, significantly increase the volume occupied by the experimental setup, and are themselves quite expensive.

2. Specific Components for Gridded Ion Thrusters

A unique component of microwave-discharge ion thrusters is the DC block. The discharge chamber must be maintained at high potential (screen voltage), whereas the microwave power source should operate near the spacecraft common potential. The DC block enables the transmission of microwave power while blocking DC voltage. It is important to note that the DC block must isolate both the hot side (inner conductor of the coaxial) and the return side (outer conductor) of the microwave line. Although DC blocks are also used in general industrial applications, the authors have not found any commercial products that simultaneously satisfy the requirements of 2 kV voltage tolerance (including margin), 10 W class microwave power handling, compact size, low mass, and vacuum compatibility. Therefore, so far all flight-proven microwave ion thrusters have used custom-designed and fabricated DC blocks. Although often overlooked, this component plays a central role in the microwave-discharge ion thruster system.

Another unique component is the vacuum feedthrough, which is not shown in Fig.12 in the case of a laboratory experiment, whereas in a flight system, the entire setup is placed in vacuum. The vacuum feedthrough is typically installed upstream of the DC block to minimize the area of high-voltage components exposed to the space where a tenuous plasma exists. Placing it upstream of the directional couplers may also be valid for more accurate microwave measurements, although this configuration increases the number of vacuum feedthroughs required for DC signals.

With the components described above, the connection from the microwave source to the discharge chamber is complete, but in actual experiments, precise microwave power calibration is indispensable. Each element in the transmission line contributes both insertion loss and reflection. Here insertion loss refers to dissipation within a device placed inline. In systems composed of multiple connected components, including vacuum feedthroughs, forward and backward waves interfere throughout the system. As a result, the forward and backward power measured at the output of the microwave source does not accurately reflect the powers that are actually transmitted to the discharge chamber. Therefore, accurate power calibration is essential for microwave power systems.

A typical calibration method involves replacing the discharge chamber with a calibrated attenuator and measuring its output using a power meter. Since most power meters are rated only for mW-level input, directly applying W-level microwave power can lead to immediate failure. This mistake has been repeatedly and expensively observed in experiments. Forward power calibration is performed by correlating the detected voltage from the directional coupler with the power meter output. To calibrate the reflected power, a full-reflection load (short or open) is substituted in place of the discharge chamber, and the relationship between the backward and forward detector outputs is measured. If the relationship between the forward detector voltage and the actual forward power upstream of the discharge chamber is known, then the reflected power can be determined under the assumption of full-reflection. However, during actual ion thruster operation, the discharge chamber is not a perfect reflector. Some of the reflected wave is re-reflected within the line and reappears as forward power, following a different path than that in the calibration setup. Therefore, to evaluate the reflected power (backward power) accurately, the directional coupler should be inserted as close as possible to the discharge chamber.

3. Others

Finally, three measurement instruments are either essential or highly useful when constructing microwave experimental systems: the power meter, the vector network analyzer (VNA), and the spectrum analyzer. The power meter, as mentioned above, is indispensable for power calibration and is a required device when used in combination with an attenuator. The vector network analyzer may not be strictly necessary, but it is an extremely efficient tool if available. This instrument measures the S-parameters of components that represent four power characteristics of a two-port device: S₁₁ is the power reflection ratio from port 1 to port 1; S₂₁ is the transmission power ratio from port 1 to port 2; S₁₂ is the transmission power ratio from port 2 to port 1; and S₂₂ is the power reflection ratio from port 2 to port 2. The VNA allows for the evaluation of component integrity and actual transmission characteristics. Furthermore, since it provides not only power ratios but also phase information, it can be used in the development of



resonators and tuning circuits. The spectrum analyzer is used to verify the center frequency and spectral spread of the microwave signal, serving as a measure to confirm the health of the microwave source. While not strictly essential, it is reassuring to have one available.

B. 10-cm-class microwave ion engines (discharge chamber size > microwave wavelength)

1. Discharge chamber (ion source)

Figure 13 shows the schematic of the thrusters, left is the first flight model onboard Hayabusa, right is the Hayabusa2's FM. As it shows, the μ 10 thruster basically consists of a 4.25 GHz waveguide, a discharge chamber, a three-grid system, and a microwave neutralizer⁷⁰. Inside the thruster, there is a microwave antenna and a propellant inlet at one end of the waveguide. In the discharge chamber, xenon electrons are continuously accelerated by electron-cyclotron resonance (ECR) heating of the microwave and a mirror magnetic field generated by two rings of samarium–cobalt magnets. By subsequent electron–neutral and electron–ion collisions, ECR plasma is formed. In the Japanese asteroid sample returner “Hayabusa2,” additional propellant inlets were installed in the vicinity of the ECR region shown in Fig.13 right, and the grid system was also modified based on the increase in ion production. To maximize the beam current keeping Isp 3000 sec, it has been found that the best way is to distribute the propellant between a waveguide inlet and discharge chamber inlets.

In the latest model for asteroid fly-by mission DESTINY⁺ scheduled in 2028, the design of the discharge chamber has been changed shown in Fig. 14^{71,72}. As Fig. 14a shows, the Hayabusa and Hayabusa2 flight model's outer magnet ring is placed at a 45-degree angle, however that of DESTINY⁺ is placed horizontally shown in Fig. 15b. This design change was effective to increase the plasma production volume and resulted in increased thrust force. A summary of the specifications of the μ 10 thrusters are shown in Table 1.

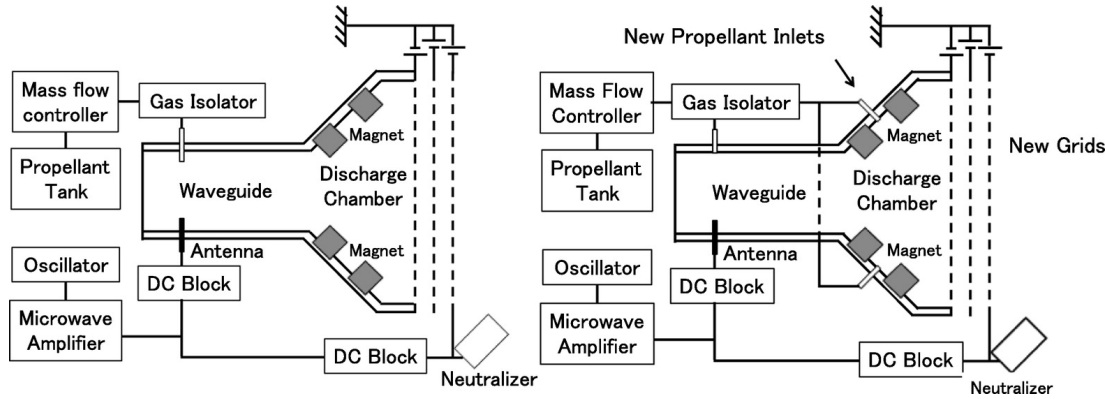


Figure 13. The schematic of the μ 10ECRion thrusters: (left) Hayabusa flight model of μ 10 thruster; (right) Hayabusa2 flight model. Compared with the Hayabusa flight model, the Hayabusa2 model has a thinner screen grid, a small hole accelerator grid, and additional propellant inlets between the magnet rings in the discharge chamber⁷⁰.

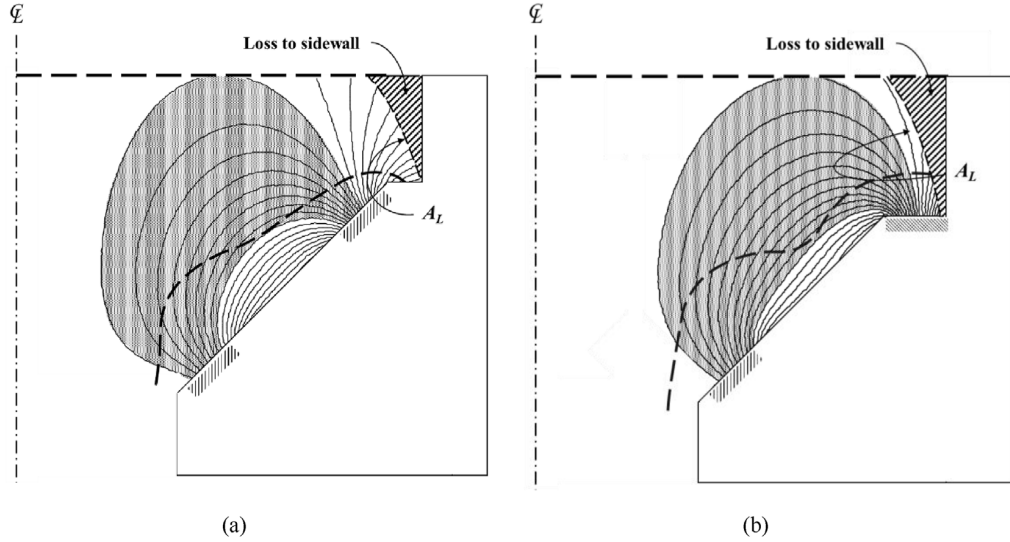


Figure 14. The schematic of the magnetic design change. (a) shows Hayabusa and Hayabusa2 flight model, (b) shows the successor mission DESTINY⁺. The angle of the outer magnet ring is modified from 45 degree to 0 degree. Dash line shows the ECR heating^{71,72}.

There are some special considerations for the use of the microwave thruster. Firstly, the magnetic field intensity is relatively higher than other gridded ion thrusters, such as RF, Kaufmann, and Ring-cusp. In case of the μ 10 thruster, 0.15 T is necessary for 4.25 GHz ECR heating. Hence, the electrons are highly magnetized, situated in the vicinity of the magnets. Fig. 15 shows the ion current density distribution of the μ 10 thrusters⁷³. As it shows, the highest peaks were recorded at the downstream of two magnets rings in all flight models. In addition, the result shows the asymmetry effect. Compared to the peak at -45 mm, the peak at +45 higher especially in DESTINY+ model. Figure 15 right is the 2D map of the DESTINY+ ion current density. As it shows, the highest ion current density is in the top right region. It is experimentally known that the highest density area matched with the position of the antenna in the waveguide. The result shows that the center of thrust does not match with the center of mechanical design. In case of the cluster operation, the discrepancy of the thrust center produces a roll torque around the thrust axis. The use of reaction wheels and the unloading of the wheels by chemical thrusters is necessary.

In addition, the roll torque is generated even in case of the single thruster operation due to the magnetization. Compared to the torque caused by the discrepancy of thrust center in the cluster operation, the torque is relatively lower, approximately $1\text{-}5\mu\text{N} \cdot \text{m}$. Ions and electrons are accelerated by ExB and grad-B drifts in the insource discharge chamber^{74,75}. Accelerated ions generate the roll torque around the thrust axis, which can be measured by laser-induced fluorescence spectroscopy shown in Fig. 16. As Fig. 16 left shows, the direction of the drift depends on the polarity of magnets. In References 74 and 75, the misalignment of Sc/Ac grids was also evaluated, shown in Fig. 16 green.

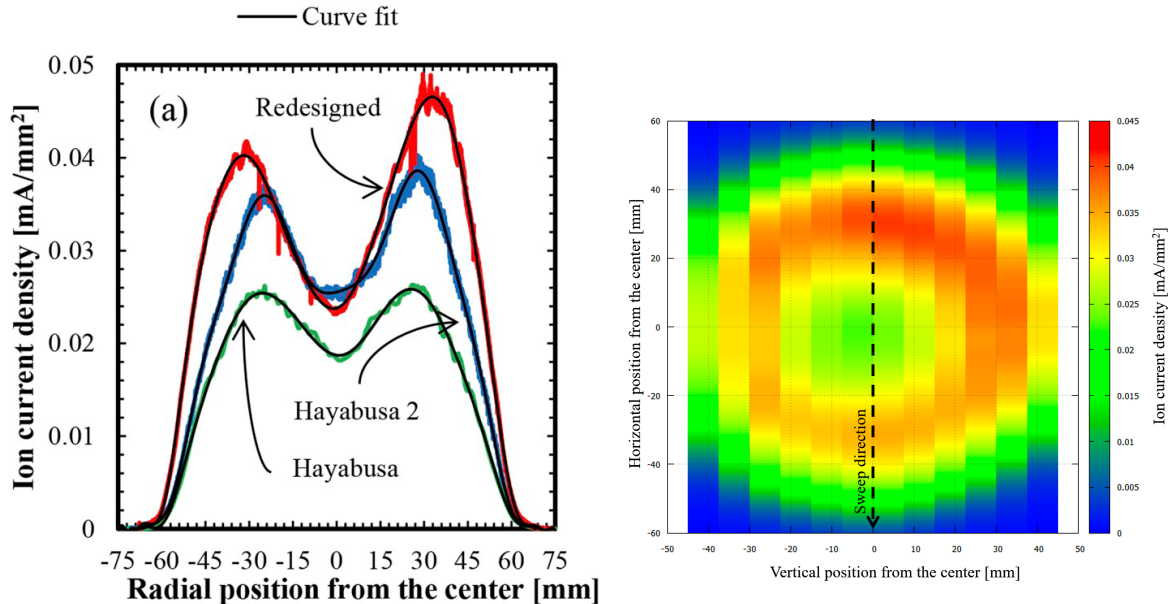


Figure 15. The ion current density distribution of the μ 10 thrusters. Left is the result of the center axis of Hayabusa in green, Hayabusa2 in blue, and DESTINY+ in red. Right is the 2d map of the DESTINY+. Dash line is the measurement line of the left figure⁷³.

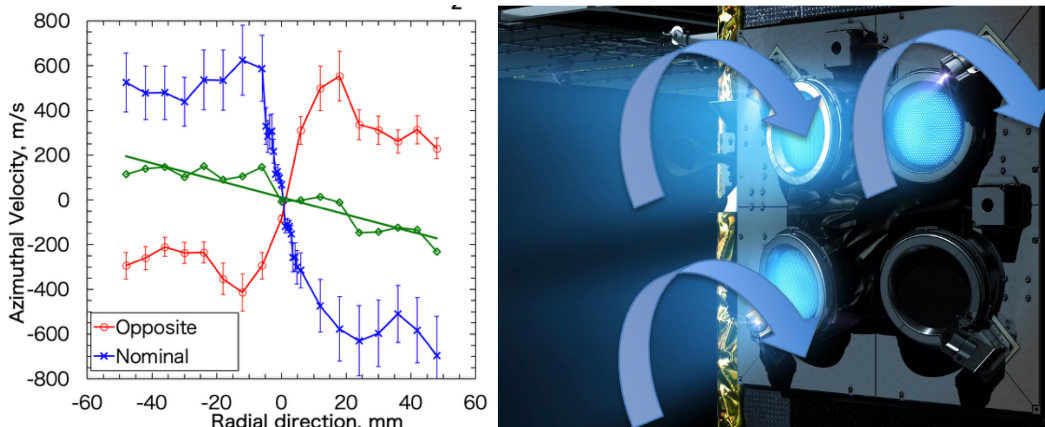


Figure 16. The Roll torque of the μ 10 thruster caused by the azimuthal ion drift in the ion source discharge chamber. Left is the results of the nominal polarity in blue and the opposite polarity in red, and the Sc-Ac grid misalignment in green. Right is the image of the roll torque^{74,75}.

Table 1: Performance of Hayabusa, Hayabusa 2, and DESTINY⁺

	Hayabusa	Hayabusa2	DESTINY ⁺
Thrust, mN	8	10	12
Ion beam current, mA	136	170	204
Specific impulse	3200	3000	3100
Discharge loss, W/A	265	200	160
Propellant utilization efficiency, %	87	81	88
Total power, W	340	400	460
Thrust efficiency	34	36	40

2. Grids and DC blocks

Unlike other ion thrusters, which typically use molybdenum grids, the “μ10” thruster uses the three C/C composite grids shown in Fig. 17 in order to minimize the sputtering yield⁷⁶. The geometry of the screen, accelerator, and decelerator grid is shown in Table 2⁷⁷. Each grid has 855 holes with a 105-mm effective beam diameter. And the screen grid has the highest open ratio approximately 70% in order to maximize the ion beam extraction, whereas the accretor grid is the lowest the open ratios from 10-20% to minimize the leakage of the neutral gas. The nominal operation voltage of screen grid is 1500V, the accelerator is -375V, and the decelerator grid is connected with the neutralizer cathode, which is typically from -20 to -30V. The thickness of the screen grid is important to improve the perveance though the beam current limiter is ECR plasma production rather than the perveance limitation. Compared to the molybdenum, the sputtering yield of the C/C composite is lower, however the mechanical strength is also lower. As a result, the thickness of the screen grid is likely to be a few times more than that of the molybdenum screen grid shown in Table 2. By reducing the thickness of the screen grid, the plasma sheath can be slightly shifted to upstream, the open ratio of ions can be improved up to 80%, which is typically higher than that of neutral particles, i.e. mechanical open ratio. Also, under the same mechanical open ratio, the smaller aperture size of screen grid is effective to improve the perveance, however the mechanical strength of the screen’s web is the limitation of the scaling down of the aperture. In the latest model thruster DESTNY⁺, the screen grid reduced the thickness to 0.50 mm, carefully considering the mechanical strength, sputtering yield and the environmental condition of the launch vehicle.



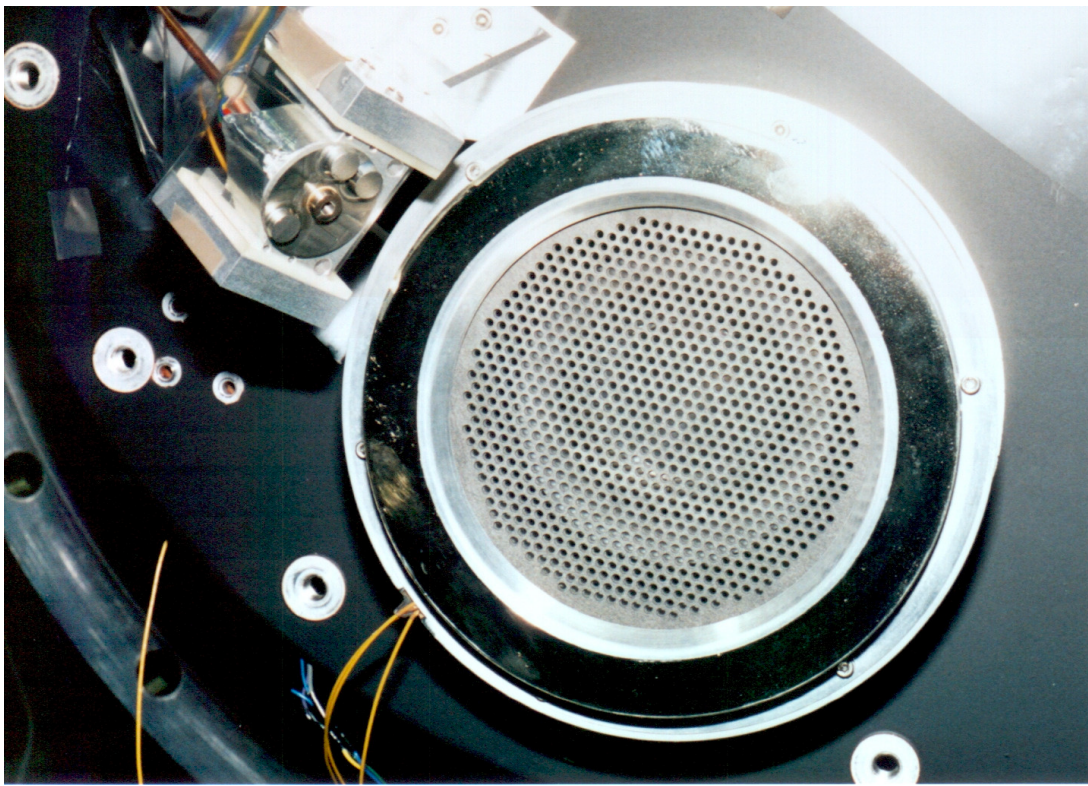


Figure 17. The C/C composite screen, accelerator, and decelerator grids with the 105-mm effective beam diameter with 855 holes⁷⁶.

Table 2: Specifications of grids system of μ 10 thruster.

	Number of holes	Voltage, V	Thickness, mm (HY/HY2/D+)	Aperture, mm (HY/HY2, D+)	Gap, mm
Screen	855	1500	0.95/0.80/0.50	3.0	0.32
Accelerator	855	-375	1.0	1.8/1.5 /1.2~1.4	0.50
Decelerator	855	Neut. Cathode (-20 to -30)	1.0	2.8	

Since the thruster is biased at 1500 V, electrical isolation must be implemented. There are the gas isolators in the propellant feeding lines. Also, the DC blocks are located in order to realize the isolation between the ion source, the neutralizer cathode and the microwave amplifier and oscillator⁷⁶. Figure 18 shows the DC blocks developed by ISAS/JAXA. Left is the developed products history from engineering models shown in top, and the flight model for the neutralizer cathode with SMA connectors shown in bottom left, and the high-power (100W) model shown in bottom right. The center photograph shows the flight model of DC block for the ion source with TNC connectors. Right is the laboratory model DC block for μ 10 HIsp with the isolation capability of 15kV, which is still necessary for the mass reduction. In case of Hayabusa and Hayabusa2, the flight model DC blocks shown in Fig. 18 are used with an efficiency of 98%.

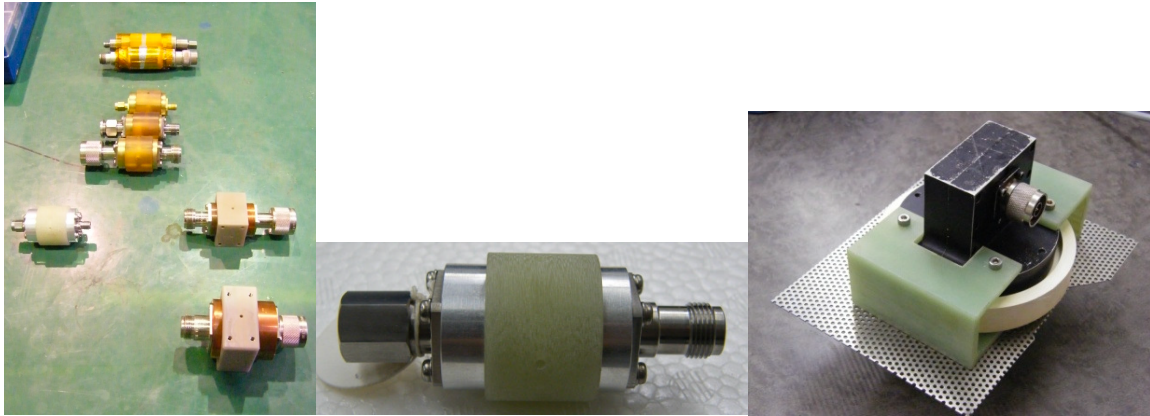


Figure 18. The photographs of DC blocks developed by ISAS/JAXA. Left is the developed products history from engineering models shown in top, and the flight model for the neutralizer cathode with SMA connectors shown in bottom left, and the high-power (100W) model shown in bottom right. The center photograph shows the flight model of DC block for the ion source with TNC connectors. Right is the laboratory model DC block for μ 10 HIsp with the isolation capability of 15 kV⁷⁶.

3. Neutralizer

Figure 19 shows the schematic of the microwave discharge neutralizer cathode⁷⁸. The cathode consists of permanent magnets, magnetic circuits, a discharge chamber, an antenna, and a nozzle. As shown in the figure, electrons are generated via two methods. In the first electron generation method, collisions between neutral particles and high-energy electrons heated by ECR at electron cyclotron frequency.

Microwaves at a frequency of 4.25 GHz are transmitted from the antenna into the discharge chamber. A magnetic circuit generates an azimuthal mirror magnetic field, within which a region with a field strength of 0.15 T gives rise to ECR heating. Xenon is injected into the discharge chamber, where electrons are continuously accelerated by microwave electrical oscillations and trapped by a mirror magnetic field due to ECR. Through electron-neutral collisions, ECR plasma is generated. During ECR heating, high-energy electrons exhibit three types of motion, namely, Larmor motion around the magnetic field lines, reciprocating motion between the magnetic mirrors, and azimuthal motion due to the curvature and grad-B drift.

In the second electron generation method, called DC discharge, the potential difference drives the electrostatic acceleration of electrons from the cathode plasma to the ion beam. The acceleration is sufficient to drive the electron impact ionization of neutrals and produces electrons for ion beam neutralization. The microwave discharge cathode generates plasma from which electrons are emitted into the ion beam by the negative applied voltage at the cathode. Ions, generated at the same rate as the ejected electrons, bombard the interior of the cathode, completing the electrical circuit.

To allow the microwave discharge cathode to be visually monitored, a part of side wall is replaced with an SiO₂ plate shown in Fig. 19 left. The magnet is moved in the circumferential direction, but the whole magnetic flux is guaranteed to be the same as the original one. The magnetic circuit supports the circumferential uniformity of the magnetic field. In addition, the orifice nozzle is partially visible through the SiO₂ plate to introduce the laser beam. To suppress the disturbance caused by the SiO₂ wall, the SiO₂ wall area is set to be as small as possible. As shown, high-density plasma was distributed along the central axis. This microwave discharge cathode can be used to continuously measure the plume region and the inside of the cathode.

Figure 20 shows the axial IVDF at the nominal operation condition of the Hayabusa2's microwave neutralizer cathode, 8 W microwave power, 0.7 SCCM Xeon flow rate, and 180 mA neutralizer current in diode mode. The numbers in the figure indicate the intensity of each velocity population normalized by the intensity at X = 0 and Z = -11 mm under nominal conditions. The numbers in brackets indicate the ratios normalized by the total intensity for the given condition. The populations include a negative-velocity population toward the upstream called "Population A" (green), a near-zero-velocity population called "Population B" (red), a positive-velocity population toward the

downstream called “Population C” (orange), and the total signal (blue). The raw data were fitted using the Voigt function. As shown in Fig. 19, a trimodal IVDF is confirmed at $X = 0$ and $Z = -11$ mm. At other positions, a bimodal IVDF is observed. At $X = 5$ and $Z = -15$ mm, the most upstream measurement point in this study, the peak velocity of Population A (about 1700 m/s) is the largest. At other positions, the peak velocity of Population A is 1200 to 1300 m/s. As shown in Fig. 12, the highest intensity is distributed at $X = 0$ and $Z = -11$ mm. At other positions, the density is about 15% of the intensity at $X = 0$ and $Z = -11$ mm. At $X = 0$ and $Z = -11$ mm, the intensity ratio is 55% for Population A, 15% for Population B, and 30% for Population C.

In Reference 78, the current oscillation was also measured. Coupling with the spectrum of the current oscillation with a monomodal Maxwellian function, the IVDFs were simulated, resulting in the agreement of the measurement. In case of the microwave discharge cathode, the operation modes are not categorized, such as spot mode, plume mode, diffusion mode in hollow cathodes, however, the operation mode of the microwave cathode has the similarity to the plume mode since there are the current/voltage oscillations and some ions are accelerated much more than operation voltage, which were also measured by RPAs.

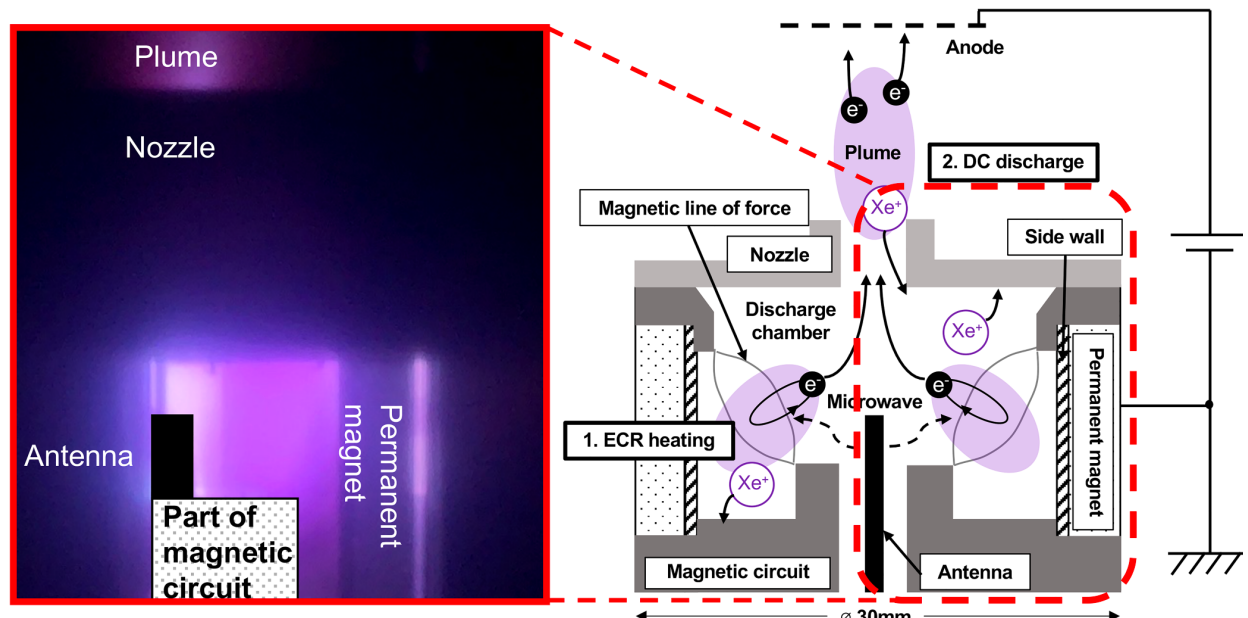


Figure 19. The schematic of the microwave discharge neutralizer cathode⁷⁸.

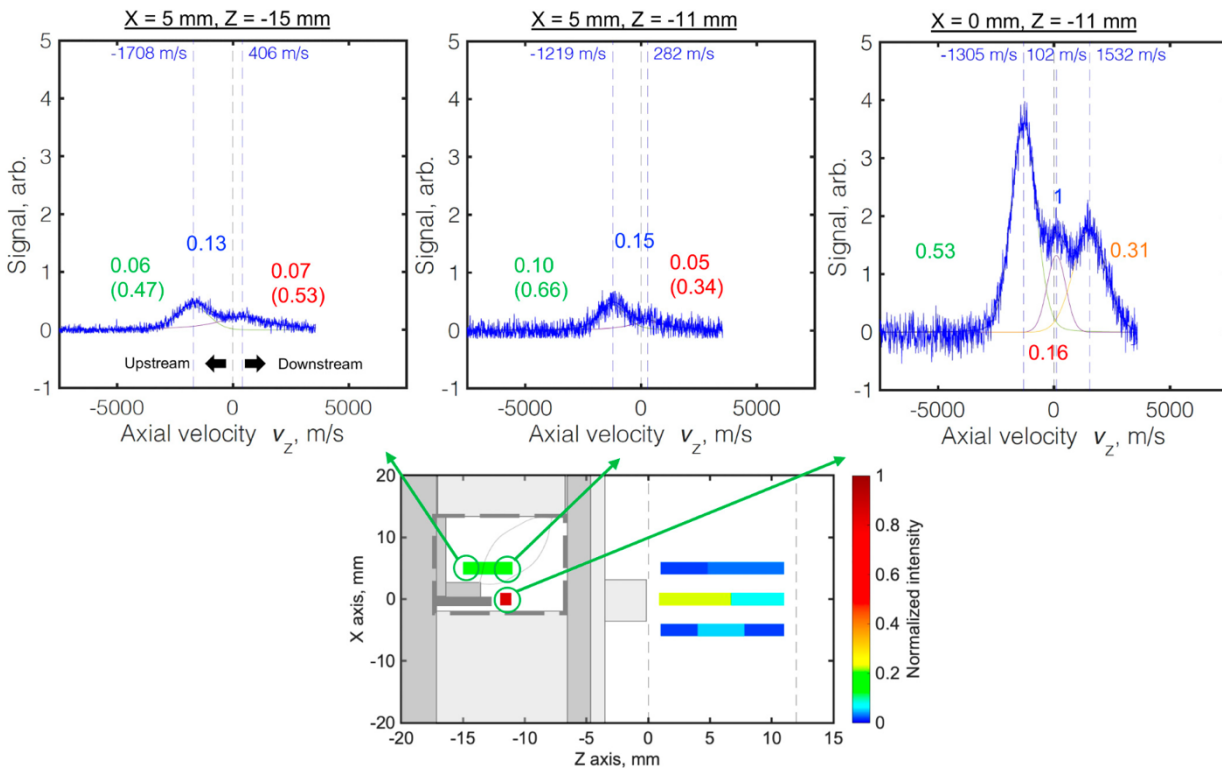


Figure 20. Axial results of LIF spectroscopy inside microwave discharge cathode at 8 W microwave power, 0.7 SCCM flow rate, and 180 mA neutralizer current⁷⁸.

XI. Diagnostic Approaches for RF Discharge Characterization

A. Introduction: Motivation and Diagnostic Objectives

Radio-frequency (RF) ion thrusters typically employ inductively coupled plasmas (ICP) to generate the ionized propellant. Power is transferred from an RF antenna to the plasma via time-varying magnetic fields, allowing electrode-less operation and enabling long lifetimes. Typical excitation frequencies range from several MHz to tens of MHz, with RF power levels between a few tens and several hundred watts.

The discharge region defines where and how ionization occurs, how efficiently energy is coupled to the electrons, and under what conditions ions are formed and extracted. As such, the plasma state within this region directly affects key thruster parameters, including ion production efficiency, beam quality, power coupling, and propellant utilization. Accurate knowledge of discharge properties is therefore essential for identifying loss mechanisms, assessing RF matching, validating numerical models, and ultimately optimizing thrust efficiency, operational stability, and lifetime. Plasma parameters in these discharges typically include electron densities from 1×10^{16} to $\times 10^{18} \text{ m}^{-3}$, electron temperatures of 1 to 10 eV, neutral pressures in the range of 1×10^{-2} to 1 Pa, and ionization degrees of a few percent. The inherently dynamic nature of RF plasmas, with time-varying sheaths and RF-modulated power deposition, poses significant challenges for both modeling and diagnostics.

Most standard diagnostic techniques provide only time-averaged or phase-integrated data. While fast diagnostics with microsecond resolution exist, they are technically demanding and often impractical in routine test environments. Consequently, the interpretation of diagnostic results - particularly ion energy distributions and species composition -



must be approached with care, considering the limitations of common assumptions such as stationary conditions or Maxwellian behavior.

Examples include:

- Retarding Potential Analyzer (RPA) measurements of ion energy distribution functions (IEDF), often interpreted assuming a Maxwell-Boltzmann distribution; this may be valid in quasi-stationary regions but not near sheaths or under strong RF modulation.
- ExB spectrometry, which reveals charge state distributions that depend on electron temperature and density, yet assumes steady-state ionization kinetics and neglects transient effects.
- Near-field Faraday cup arrays, which map the ion current density across individual beamlets; under known extraction geometry, these profiles reflect the lateral plasma density distribution.

Because each method probes only specific aspects of the plasma, no single diagnostic can fully characterize the discharge. For example, RPAs yield energy information but not species, E x B analyzers resolve species by their velocity but not energy, and Faraday cups provide current density but not temperature or potential. Moreover, interpretation often depends on assumptions that may not hold under RF-driven, non-equilibrium conditions.

To overcome these limitations, complementary diagnostics must be combined. This integrated approach enables cross-validation, reduces ambiguity, and provides a more consistent and comprehensive picture of the plasma. It is essential for understanding the dynamic behavior of the discharge, guiding design decisions, and supporting model-based optimization of RF ion thrusters.

B. Perveance Measurements

A measure to describe the ion optics of a gridded ion thruster with respect to their beam focusing characteristics is the perveance, which is defined by

$$P = \frac{I_{beam}}{U_T^{3/2}} \quad (20)$$

with I_{beam} denoting the beam current and U_T denoting the potential difference between the discharge chamber and the accelerator grid electrode. At the perveance optimum, the primary ion trajectories of a beamlet are well focused. Furthermore, it is common to use the term *over-perveance*, when focusing is too weak, which may lead to direct impingement onto the accelerator grid along some trajectories below a threshold for U_T , and the term *under-perveance*, when focusing is too strong and some ion trajectories cross over the symmetry axis, which may also lead to trajectories intercepting with the accelerator grid above a threshold for the extraction voltage⁷⁹.

A standard way to experimentally characterize the perveance of a grid configuration is to measure the accelerator grid current I_{acc} in dependence on the extraction voltage U_{ext} . For a single beamlet, beam formation, and the limits where in between no primary ion trajectory is intercepting with the accelerator surface, can be calculated with numerous numerical codes, such as CEX2D, IGUN, IBSIMU, among others⁸⁰⁻⁸². Regarding a multi-aperture grid under over-perveance conditions, the $I_{acc}(U_{ext})$ relation carries also information about the plasma density distribution across the screen grid radius: While for homogeneous plasma density distribution the threshold of U_{ext} for direct impingement is equal for every beamlet across the grid radius, a plasma density distribution peaked in the center and decreasing to larger radii can cause that, near the perveance limit, central beamlets suffer from direct impingement, while beamlets in the outer grid region do not. In this case, the voltage of the perveance limit will shift, and the accelerator grid current will grow at a lower rate towards lower voltages, compared to the conditions of a homogeneous plasma density profile. An example, using the grid erosion code DYNASIM, is displayed in Fig. 21⁸³.



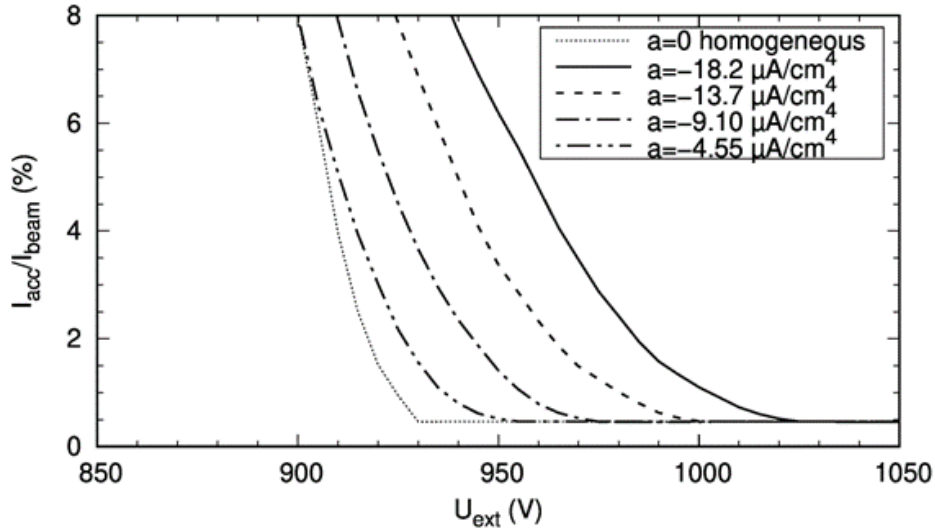


Figure 21. Simulated accelerator grid currents for a homogeneous plasma profile and a set of plasma density distribution functions. Here, the resulting current density distribution is assumed to be parabolic, the variation of the coefficient a corresponds to an increase of the beamlet current (in terms of the average beamlet current) of 5% ($a = -4.55 \mu\text{A}/\text{cm}^4$) up to 20% ($a = -18.2 \mu\text{A}/\text{cm}^4$) towards the grid center, respectively.

C. Retarding Potential Analyzer

1. Working principle and measurement setup

The Retarding Potential Analyzer (RPA) is a widely used diagnostic tool for measuring the ion energy distribution function (IEDF) in electric propulsion systems. It operates by applying a variable electrostatic potential to a retarding grid, which selectively blocks ions below a given kinetic energy threshold. The basic operating principle is illustrated in Fig. 22. By recording the transmitted ion current as a function of the retarding voltage, the cumulative energy distribution can be reconstructed; differentiation of this curve yields the IEDF.

A typical RPA consists of multiple planar grids mounted in front of a collector electrode:

- An entrance grid, which is either grounded, held at a defined reference potential or floating to beam potential. It serves to shield the analyzer from external electric fields and establishes a well-defined electrostatic boundary condition at the entrance.
- A repeller grid, biased negatively (typically up to -100 V) with respect to the entrance, to repel incoming electrons from the neutralized ion beam and prevent them from reaching the retarding region.
- A retarding grid, to which a variable voltage is applied. It acts as an electrostatic energy filter by repelling ions with insufficient kinetic energy
- An optional suppressor grid, biased negatively (typically up to -100 V) to repel secondary electrons emitted from the collector.
- A collector electrode, which measures the ion current transmitted through the retarding field.



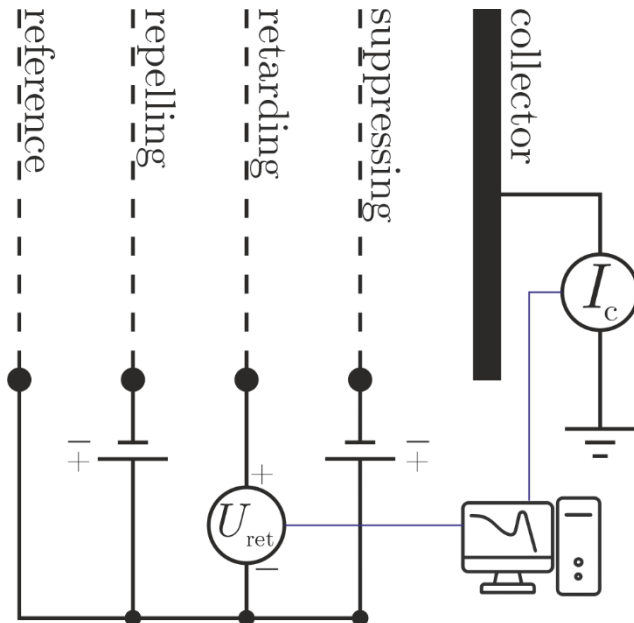


Figure 22: Schematic of a retarding potential analyzer used for ion energy distribution measurements. The setup includes a reference grid, which can be floating to either the beam potential or set to chamber (ground) potential, a repeller grid to block electrons from a neutralized beam, a retarding grid with adjustable potential U_{ret} for energy filtering of ions, a suppressor grid to reduce secondary electron emission from the collector, and a collector electrode for measuring the ion current I_c . The derivative of the ion current as a function of U_{ret} provides the energy spectrum of the incoming ions.

The device is aligned along the beam axis and positioned downstream of the thruster, typically at several tens of centimeters from the exit plane. In the context of RF ion thrusters, RPA measurements are typically time-averaged over many RF cycles. Fast modulation of plasma potential or sheath dynamics may therefore not be resolved directly but can influence the width and shape of the IEDF. The resulting data provides insight into the kinetic energy of the extracted ions, the effective plasma potential, and the quality of beam formation.

2. Determination of the Ion Energy Distribution Function (IEDF)

The primary purpose of the RPA is to determine the IEDF of the extracted plasma. By sweeping the retarding voltage and recording the resulting current, one obtains the integrated ion flux above a given energy. An RPA typically provides one-dimensional resolution of the velocity or energy distribution of charged particles. In this context, we assume a velocity distribution $f(v)$ normal to the equipotential surfaces of the retarding grid. The ion density in a differential velocity interval is then given by $dn = f(v)dv$. The average ion current I at the collector can be described by

$$I(v) = \sum_j A_c q_j e \int_{v_{\min}}^{\infty} v \cdot f_j(v_j) dv, \quad (21)$$

Where A_c denotes the effective collector area as seen by the ion beam. The integral represents the transmitted ion density in the interval $[v_{\min}, \infty]$, e is the elementary charge, q_j the ion charge state and U_{ret} the retarding potential. Using the relation $v = \sqrt{2q_j e U / m_i}$, the average ion current can also be expressed as a function of the retarding voltage. This ultimately allows the derivation of the current variation with respect to the voltage, yielding the differential form



$$-\frac{dI(U)}{dU} = \sum_J \frac{A_c q_j^2 e^2}{m_i} f_j(U). \quad (22)$$

From this expression, it becomes evident that the negative derivative of the measured collector current with respect to the retarding voltage is directly proportional to the voltage distribution function of the particle beam. If all particles in the beam share the same mass and charge state, the voltage distribution function $f(U)$ can be directly equated to the energy distribution function $f(E)$, using the relation $U=E/(qe)$. However, if the beam consists of particles with identical mass but different charge states, the RPA yields only the distribution of the energy-to-charge ratio. Consequently, ions with different charge states cannot be distinguished by the RPA.

Accurate interpretation of RPA measurements requires careful consideration of systematic uncertainties and device-specific effects. One major source of error stems from the transparency and spacing of the grids, which affect both the energy resolution and the transmission function of the analyzer. Non-uniform grid potentials and fringe fields can lead to partial energy filtering or angular deflection of ions, especially at low energies. Secondary electron emission from the collector surface - induced by ion impact - can artificially increase the measured current, particularly if not sufficiently suppressed by a biasing grid. The suppression efficiency depends on the grid potential, geometry, and electron energy, and may vary with operating conditions. Contact potentials between dissimilar materials or work function differences between electrodes and grids can introduce small but non-negligible offsets in the effective retarding voltage. These must be accounted for through calibration, typically by comparing the RPA response to a known monoenergetic ion beam or by referencing the energy axis to well-defined acceleration voltages. Further errors may arise from misalignment with respect to the beam axis, resulting in angular broadening or reduced collection efficiency. In beam experiments, careful alignment, shielding, and background subtraction are essential to minimize such effects and to ensure reliable extraction of the IEDF. Where possible, numerical modeling of the electrostatic field geometry can support the correction of systematic distortions in the measured energy spectra.

The interpretation of RPA data is based on several simplifying assumptions that may not hold under all experimental conditions. A common assumption is that the ion velocity distribution function $f(v)$ is one-dimensional and aligned normal to the equipotential surfaces of the retarding grid. This presumes a well-collimated, mono-directional beam and neglects angular spread or transverse ion motion, which can arise from extraction optics, space-charge effects, or plasma instabilities. Furthermore, the derivation of the IEDF typically assumes collisionless transport through the analyzer and neglects space-charge interactions within the RPA itself. At high beam currents or low ion energies, mutual repulsion between ions can lead to beam broadening, energy shifts, or partial reflection, thereby distorting the measured spectrum. In addition, the analytical relation between the derivative of the collector current and the energy distribution assumes a steady-state, stationary plasma. In RF plasmas, time-dependent sheath dynamics and potential fluctuations can violate this assumption, resulting in apparent broadening or modulation features in the IEDF that may not reflect thermal ion distributions. Finally, if multiple species or charge states are present, the resulting energy-to-charge ratio spectrum represents a convolution of different contributions, limiting species-resolved interpretation unless complemented by additional diagnostics such as ExB spectrometry.

IEDFs in RF ion thrusters are usually dominated by singly charged ions (e.g., Xe^+), and the energy distribution reflects the sum of the plasma potential and the extraction voltage. In the ideal case of monoenergetic ions from a well-defined plasma potential, the IEDF exhibits a narrow peak. Broadening of the distribution may result from ion-neutral collisions, plasma fluctuations, RF sheath modulation, or angular spread at the extraction grids. These processes are illustrated in Fig. 23.

3. Key insights:

- Plasma potential estimation: The energy offset of the main IEDF peak with respect to the known extraction voltage allows for estimating the effective plasma potential. This is particularly valuable in RF systems, where time-varying sheaths complicate direct potential measurements.
- Ionization efficiency: The total integrated ion current measured by the RPA provides a measure of the extracted ion flux. Combined with propellant flow rate and charge state information (e.g., from E x B analysis), it allows estimation of the degree of ionization and overall efficiency.



- RF energy coupling and modulation features: Deviations from a monoenergetic distribution - such as shoulders, secondary peaks, or broadened structures - can indicate the presence of RF modulation effects, non-equilibrium sheath dynamics, or multiple ionization pathways. In some cases, harmonics of the RF drive may be visible in the IEDF as periodic modulations.
- Ion temperature and energy spread: The width of the IEDF peak near its maximum can be related to the ion temperature, assuming a thermal component superimposed on directed motion. However, in RF systems, this spread may also include contributions from time-varying sheath potentials or angular effects.
- Sensitivity to discharge matching conditions: Changes in RF matching, power level, or operating pressure are reflected in the shape and position of the IEDF. For example, poor matching may lead to reduced plasma potential, lower peak energies, or increased spread due to unstable sheath behavior.

4. Plasma potential and electron temperature

Retarding Potential Analyzer (RPA) measurements provide direct access to the energy of the extracted ions. In RF ion thrusters, this energy of extracted ions is determined by the sum of the plasma potential and the externally applied acceleration voltage. The position of the maximum in the IEDF corresponds to the most probable ion energy, E_{ion} . The plasma potential V_p relative to the screen grid potential can thus be estimated by

$$V_p = V_{ion} - V_{accel}, \quad (23)$$

where V_{accel} is the known acceleration voltage between the screen grid and ground and V_{ion} is given by E_{ion}/e assuming singly charged ions. This effective plasma potential reflects the average floating potential of the plasma, which arises from the balance



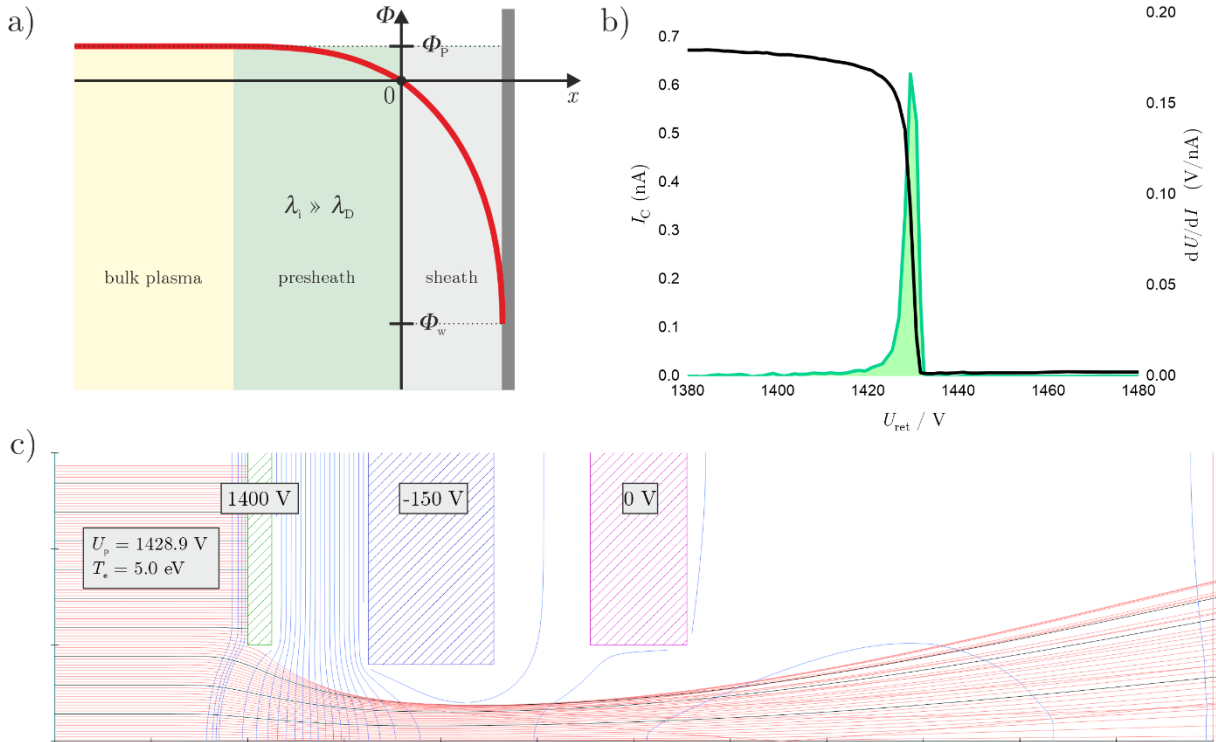


Figure 23: a) Schematic illustration of the electrostatic potential profile near a plasma-facing surface, showing the bulk plasma, presheath, and sheath regions. The potential drop occurs mainly across the sheath, but the presheath establishes the ion flow conditions required to satisfy the Bohm criterion. b) Example of an RPA measurement for an applied acceleration voltage of 1400 V. The ion energy distribution reveals a peak at approximately 1429 V, indicating an energy shift of about 29 eV above the nominal acceleration voltage. c) Simulation illustrating the origin of this energy shift because of the plasma charging relative to the extraction system. The observed shift corresponds to the sum of the floating and plasma potential and correlates with the local electron temperature, here estimated to be 5.0 eV.

between electron and ion currents to the walls. In electropositive plasmas with Maxwellian electrons and cold ions ($T_i \ll T_e$), the plasma potential V_p relative to the screen grid potential is given by

$$V_p = T_e \left(\frac{1}{2} + \ln \left(\sqrt{\frac{2\pi m_e}{m_i}} \right) \right) \quad (24)$$

with T_e in eV, electron mass m_e and ion mass m_i . Solving for T_e gives

$$T_e = \frac{V_p}{\frac{1}{2} + \ln \left(\sqrt{\frac{2\pi m_e}{m_i}} \right)} \quad (25)$$

Thus, by measuring the energy offset between the applied voltage and the peak ion energy, and inserting the known ion mass, one can estimate the electron temperature.

For xenon ($m_i \approx 131$ u), the factor $\frac{1}{2} + \ln \left(\sqrt{\frac{2\pi m_e}{m_i}} \right)$ is approximately 5.8, so

$$T_e \approx \frac{V_p}{5.8} \quad (26)$$

This estimation provides a non-intrusive method to determine T_e in RF plasmas. Once T_e is known, it enables further calculations of key plasma properties such as Debye length, sheath thickness, ion sound speed, and Bohm current. In



combination with ion current density or ion flux measurements, RPA-derived T_e becomes a powerful tool for assessing plasma density, energy balance, and discharge efficiency of the thruster.

XII. Micro Gridded RF Ion Thruster

A. Micro Gridded RF Ion Thruster: Introduction

The past decade has seen unprecedented levels of growth in the market for small satellites, particularly in the MicroSat class (10-100 kg). While demand for all micro satellites has risen as a result, the “medium” sized, 20-50 kg MicroSats (including 12U and 27U CubeSats) have seen a marked increase in demand in recent years. Like all small satellites, the cost of MicroSats has decreased due to more affordable subsystem components, decreased launch costs, and the advent of ridesharing. At the same time, these satellites support substantial mission-enabling payload volumes and are highly configurable. This ideal balance between low cost and sufficient capability has made the 20-50 kg MicroSats appealing for a wide array of commercial missions.

The increasing popularity of these medium-sized MicroSats demands low cost, high performance, and compact propulsion systems. Within all electric propulsion (EP) solutions, micro gridded RF ion thrusters have gathered a lot of traction due to their moderate thrust ($\sim 1\text{mN}$), high Isp ($\sim 2,000\text{sec}$), and relatively low power consumption ($<80\text{W}$). The unique ability of RF ion thrusters to use solid iodine as propellant further adds to their appeal. Small RF propulsion system characterization is similar to that of larger engines described previously with some considerations related to size discussed in subsections below.

B. Micro Gridded RF Ion Thruster Neutralization

Due to their low overall propellant consumption, micro RF ion thrusters are seldom coupled with gas fed hollow cathode neutralizers for flight missions. Instead, hot filaments have been proven sufficient (by ThrustMe), although they are less scalable in both emissive current output and total duration⁸⁴. An alternative approach is to use an inductive RF cathode as the neutralizer, a practice that did not gain flight heritage until Busek’s BIT-3 missions.

When testing micro RF ion thruster neutralization on the ground, the most important aspect is to avoid inadvertent ion beam grounding by the vacuum chamber walls. If the chamber is too small, the thruster plume can be sustained even without a cathode neutralizer, creating a false sense of neutralization. In this scenario the cathode’s ability to emit electrons cannot be assessed accurately, which may lead to a charge imbalance risk during flight. This is especially important because neither filament cathodes nor RF cathodes produce overwhelming electron emissions like hollow cathodes do, so the ground test should be carefully set up to verify proper neutralization⁸⁵. A general rule for avoiding such problems is to choose a vacuum chamber large enough that its wall diameter is at least 20x of the thruster grid’s diameter, and its length is sufficiently long that there is at least 1 meter of axial separation between the thruster grid and the wall. Coating the beam-impinging wall with an electrically-insulative material such as PTFE can also help isolate the ion beam. In practice, the simplest way to check whether the beam is coupled to the chamber wall is to momentarily turn off the cathode while the thruster is firing. If the ion beam immediately terminates or becomes unstable, or if there is significant arcing in the vicinity of the thruster, it is evidence of charge imbalance. This indicates the test setup is adequately shielded from the chamber walls.

C. Micro Gridded RF Ion Thruster Propellant Injection

Propellant injection for micro RF ion thrusters follows standard propellant management practices for larger gridded ion thrusters. For noble gases, bang-bang controlled or proportionally controlled solenoid valves reign supreme. For iodine propellant, the gas flow rate is controlled by heating the solid iodine reservoir, along with various feedback regulation mechanisms. One design aspect seldom discussed is the injector fitting isolation and choke. Because micro RF ion thrusters use ceramic discharge chambers, designers are often unaware that the injector fitting (typically made of metal) can float up to 1kV or 70-80% of screen grid potential during normal operations. This is caused by the RF plasma acting as a conductor and electrically connecting the injector fitting to



The 39th International Electric Propulsion Conference, Imperial College London,
London, United Kingdom 14-19 September 2025

Page 38

Copyright 2025 by the Electric Rocket Propulsion Society. All rights reserved.

the screen grid. If left untreated, it can cause many problems as “shorting” with cathode current, overheating and causing gas seals to melt. Another common problem stemming from the injector fitting’s floating potential is gas breakdown within the feedline. Grounding the injector fitting is obviously not a solution because the fitting is electrically tied to the screen grid when the thruster is firing. Possible mitigation choices include the use of a ceramic spiral isolator to increase the gas pathlength, d , of Pd in the Paschen curve, installing an orifice choke point to increase the pressure part of Pd in the Paschen curve, or both.

D. Micro Gridded RF Ion Thruster Power Supply

One of the most challenging aspects of any micro RF ion thruster’s PPU is its RF power amplifier. In a typical Class E amplifier circuit design, high DC-to-RF conversion efficiency can be achieved, but usually only within a very narrow frequency band (i.e. $\pm 200\text{kHz}$) and under a specific load condition (i.e. 50Ω impedance at high power output). Deviating from those conditions can cause the efficiency to drop noticeably, exemplified by Fig. 24. Some efficiency can be recovered by utilizing non-fixed drive frequency with automatic impedance match via PPU control. This would require digital synthesis of the drive frequency and a software logic that constantly sweeps the drive frequency to find the optimum impedance match point, evidenced by the lowest RF power reflection.

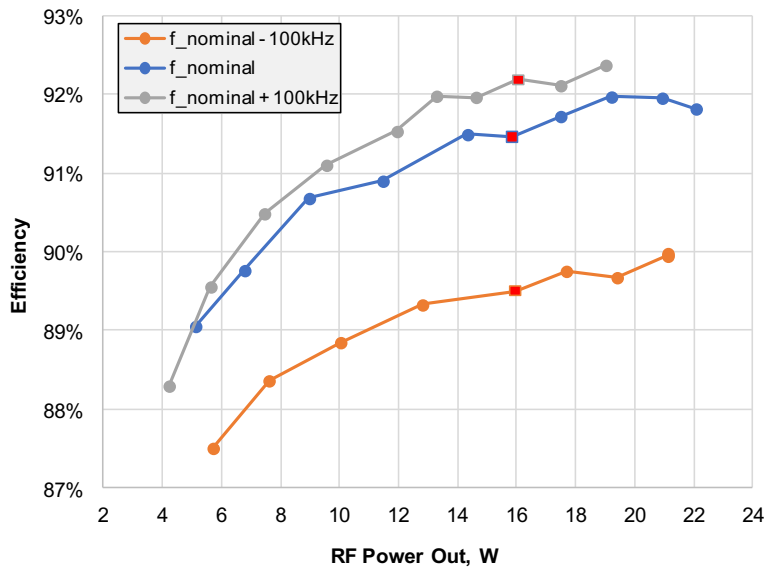


Figure 24. DC-to-RF Conversion Efficiency Chart of Busek’s BIT-3 RF Power Amplifier

XIII. Assembly and Chamber Considerations

Setting up the apparatus to mount the thruster, probes and translation stages is a significant undertaking as components need to be vacuum compatible. Handling of components requires the use of appropriate protective clothing, gloves, shoe covers to limit contamination. Bare hands for example contain oils and other contaminants that can interfere with operation of both thruster and probes. Ideally, components in the chamber should be of quality like what one would actually fly to avoid ground test specific results. Ultimately, using lower-fidelity components for testing may lead to increased development costs as these components may produce results which deviate significantly from flight conditions, necessitating additional (higher-fidelity) ground testing. In this subsection we review basic considerations regarding vacuum hygiene and materials considerations. Use of proper materials in the chamber avoids outgassing



which can degrade your vacuum, poison a process or component such as a hollow cathode, and deposit films on surface such as probes or anode. Such resistive layers lead to shifts in data curves such as the IV characteristic of a Langmuir probe and thus lead to erroneous interpretation of data. Here we review very briefly considerations for a clean vacuum for thruster operation.

A. Structural components

Anodized materials which can be used for support structure fabrication are porous and can soak up water which evolves into the background plasma and thruster if not properly managed. These structures have an outgassing rate of ~400 times that of regular aluminum after pumping for 24 hours⁸⁶. Concerning commercially available anodized materials designed for building structures for mounting thrusters and probes, it must be noted that such surfaces are structurally sound but are not truly grounded which means such structures can charge and alter results. Convenience and “test as you fly” do not overlap. Often ground leads are attached to anodized aluminum leading to an ambiguous reference. These materials have high resistivity and can lead to spurious results if not used properly. Anodized materials should be either avoided or processed to assure reasonable conductivity and elimination of porosity. Lessons learned regarding a NASA perspective may be found at <https://llis.nasa.gov/lesson/8403>. Additionally, NASA maintains a database for electronic parts and packaging. Such a database is useful to assess whether to use a particular component or material in the vacuum chamber: <https://nepg.nasa.gov/>. Fasteners should be stainless steel as plated materials can become contamination sources. Cadmium and zinc for example are cathode poisons. The materials should be avoided owing to their high vapor pressure. Often fasteners and ring terminals are plated with these materials. So note coatings of even stainless fasteners Many variants are coated and thus not appropriate for vacuum/thruster duty. Materials used for space applications are documented in NASA-STD 6016 and one should strive to incorporate these materials into their setups. If you are unsure of the limits of a particular material, then utilize the MAPTIS database: <https://maptis.nasa.gov/>. Charging effects can lead to arcing and damage to wires and electronics. To avoid such events, overuse of Kapton tape and mica shielding and other dielectrics should be minimized. All cable shields should be grounded to the chamber-either mechanically or vacuum grade solder. Metalized foils are not desirable for grounding. Coax cables are not sufficient if the ground braid is not grounded to the facility. Also be aware of the “red plague” which occurs on exposed silver covered copper. It is a chemical effect leading to corrosion thus reducing the effective cross section of your wire (effective gauge change). The process occurs due to the presence of water and oxygen—the corrosion process proceeds indefinitely. It can be identified by reddish color on the wire-copper oxide (for additional details see ECSS-Q-ST-70-20C). Poor crimping technique and lack of wire storage in a reasonable environment can contribute to the red plague. In general, poor crimping is problematic for any test—proper technique and the appropriate sizing of wire to the ring terminal are paramount. Proper tools for a solid crimp is critical. Any adhesives should also be vacuum rated-satisfied by NASA ASTM E595 and may be found in NASA outgassing database. Blind holes and potential trapped air sources should be avoided.

B. Wire

Wire should be vacuum rated. Conventional wire has trapped air between insulation and wire core and thus it constitutes a slow air leak source. If the wire is at high voltage then it can lead to breakdown. The effect of sustained plasma formation due to trapped air in wire is believed to be the mechanism behind the sustained operation of a space tether after it snapped from the shuttle⁸⁷. Teflon coated Kapton wire is a good choice for vacuum chamber wiring. There are some variants of heat shrink tubing that are also vacuum compliant such as Suitube B2. NASA maintains a database on outgassing considerations for greater detail: <https://etd.gsfc.nasa.gov/capabilities/outgassing-database/>. Finally, one must be made aware of tin “whiskers” that can form on tin plated wires (typical of conventional wire to protect copper from corrosion) and from solder connections. Here tin filaments or whiskers can grow from the surface—the mechanism of growth is not well understood—which can lead to shorting especially if connections are too close or even initiate arcing events. Macor and BN are good ceramics for vacuum duty but note that BN is hydrolyzed by water and should be baked out before use. Before materials are placed in the chamber they should be cleaned to remove contaminants. A typical cleaning procedure is alcohol followed by acetone in an ultrasonic bath to



remove hydrocarbons and wiped with lint free wipes. As a final note, if the system has been exposed to air for approximately 24 hours, some form of bake-out procedure is recommended. Gas feed systems exposed to air should also be baked out. The feed system is an important consideration as it transports propellant into the vacuum chamber. The history of the tubing—stainless—should be known, particularly how its manufactured as deposits of contaminants can be absorbed on its inner surface—this is why electropolished tubing is desirable for tubing to assure a smooth inner surface that is relatively free of surface contamination. The duration and time of bake out depends on test requirements. Typical leak rates high vacuum systems well baked out systems are of order 10^{-9} Torr/min. As a final note, care must be taken in set-up if one's measurements are to be meaningful.

C. Back sputtering

Graphite is typically used as armor to protect the walls of the chamber which can be aluminum or stainless steel. The beam dump is usually also made of graphite. While this material has a low sputter yield it is porous and absorbs water. The interaction of the energetic ion beam with graphite surfaces generates a plasma composed of secondary electrons, graphite, water, and water-derived ions such as OH. This soup generates other hydrocarbons which can coat probes and engine components leading to increased resistivity. The problem is well known in the fusion community. In the fusion community, the graphite is typically baked out at 350 C. Surface morphology of graphite also changes as pores are clear out during bake out—suggesting sputter yield may be different depending on whether the substrate is baked or not. Baking out the graphite may be necessary for stability in sputter rate over a given test⁸⁸.

The thruster is important but ancillary systems connected to the engine and the chamber itself will influence engine operation and its lifetime. Mil-Spec should be a guide for off the shelf parts where vacuum compatibility is in question. And always routinely take a pump down curve to characterize the health of your chamber. Variations in the pump down curve could mean leaks, the need for a longer bakeout, or pump performance degradation such as pump oil change or the need for cryopump recycling.

D. Facility Layout

Considering appropriate test facilities for ground testing can help alleviate some of the pressure related facility effects. One of these important considerations is the size of the facility. For guidance, the 30,000 hours Deep Space 1 life test was performed in a test facility that was 3 m in diameter and 10 m in length⁸⁹. A modified NEXT engineering model (EM3) thruster has been successfully operated for over 50,000 hours for the NEXT Long Duration Test with more than 900 kg of xenon processed at the NASA Glenn Vacuum Facility-16 (VF-16)⁹⁰. VF-16 is 2.75 m in diameter and 4.5 m in length. Simulation models by Wang et al. suggest that chamber walls should be at least several beam radii from the thruster and the thruster beam to limit facility wall effects on the thruster operation⁹¹.

There are other important considerations for controlling background pressures. The location of pumps and objects in the plume can also have a significant impact on pumping speeds and local pressure gradients. Yim et al. and Lipscomb et al. have shown there are local pressure gradients that arise based on pump locations and propellant flow rates^{92,93}. Facility pressure simulations that model propellant flow rates and pump locations are recommended to optimize the pumping speed of a facility. Objects placed in front of pumps can drastically reduce the effective pumping speed of a facility. However, direct contact of high energy ions on cryogenic pumps can heat and knock off already captured particles. Panels are sometimes placed to protect pumps from this effect. Taghizadeh et al. demonstrated that reflection angles of these panels and the beam target shape can be optimized to protect pumps, and they can be used to limit sputtering and particle fluxes back to the thruster⁹⁴. Measurements of background pressure should follow the recommendations outlined by Dankanich et al in Ref. 95.

With the rise in the use of alternative propellants it is also important to consider things like the corrosiveness of the propellant and the sticking coefficient between gas particles and the pumping surface. Cryogenic pumps lose efficiency as the condensability of the gases they are tasked in pumping decreases. Turbomolecular pumps are often used to extract these other species. Diffusion pumps have all been eliminated from service due to oil backstreaming contamination. Furthermore, impurities in materials can cause significant outgassing or sputtered contaminants to be released due to the ion beam. Topham showed there are elevated hydrocarbon species that are present only when the beam is on and is directly bombarding a flexible graphite beam target⁹⁶. These hydrocarbons and impurities were also



shown to contaminate probes and cause other issues. Careful consideration of where materials are placed in the chamber and their exposure rate to high energy particles must always be considered to mitigate the flux of contaminants back onto the thruster.

E. Thruster Chassis and Plasma Screen

For steady state operation, current and charge neutralization is required otherwise the discharge chamber will charge up and the beam will turn back on the thruster or spacecraft body. In space or in a vacuum chamber, in practice if the neutralizer is not functioning, this may result in field emission from nearby structures. These take the form of cathode spots which can lead to erosion of nearby structures. In spaceflight, this will damage the spacecraft. Incomplete neutralization also reduces the potential difference between the beam voltage and beam potential, which reduces thrust as well (Fig. 4). Charge neutralization means the beam is quasineutral and current neutralization means injected electron current—ideally from the neutralizer—into the beam equals the ion beam current. In space, the beam is the only potential for the neutralizer electrons to be drawn to, but during ground testing other competing pathways for current neutralization can occur. Such competing pathways means the neutralizer operating condition in ground tests would not be the same as in spaceflight. For this reason, the way the thruster is electrically incorporated into the test facility is critical to ensuring reliable results can be produced by ground testing.

To achieve proper ground testing results, the thruster should be electrically configured in the test facility as similarly as possible to the spaceflight configuration. In space the thruster is powered by a power processing unit (PPU). The PPU can be configured in variety of ways. Inadequate neutralization causes the potential difference between the neutralizer and beam to drift to higher voltages and forces the neutralizer cathode into plume mode. Typically, a Zener diode is placed between neutralizer common and spacecraft or facility ground to prevent the neutralizer from floating too far from ground. The thruster chassis (which contains the mounting structure) is typically tied to spacecraft ground. There is no *true* ground in space so the chassis and spacecraft ground, regardless of how the PPU and thruster are configured, are electrically floating in the ambient plasma. During ground testing, the thruster and the plasma are surrounded by chamber walls and the plasma screen which establish a strict Dirichlet boundary condition. To obtain a more realistic coupling voltage, it is best to have the plasma screen floating to avoid neutralizing electrons from bypassing the beam and flowing to the plasma screen.

The plasma screen is the outer mesh that surrounds the anode and the other internal components of the thruster. It acts as a shield for these internal components such that the ambient plasma does not cause damage or interfere with the operation of the thruster. In spaceflight, the plasma screen is either electrically isolated from the thruster chassis and independently electrically floating in the ambient plasma or it is tied to spacecraft ground, which is also electrically floating in the plasma with the whole spacecraft.

In ground testing some past experiments have grounded the plasma screen to facility ground. Unfortunately, this connects the plasma screen with the chamber walls and leads to enhanced coupling with the facility. Patterson et al. found that proper characterization of the neutralizer could not be performed due to electron collection on the grounded plasma screen⁹⁷. In their work, it was determined that electrons collected on the grounded plasma screen were completing the neutralization circuit as the beam terminated on the grounded beam target. Topham et al. confirmed that grounding the plasma screen affected the operation of their thruster in their experiments^{96, 98, 99}. They demonstrated that the facility and true coupling voltages vary between an electrically floating and grounded plasma screen due to changes in the plasma potential in the beam and alternative neutralization pathways which arise with a grounded plasma screen. While the potential of neutralizer common and ground is often taken as a surrogate for the coupling voltage, the true coupling voltage may be obtained using an emissive probe. Here the emissive probe measures the plasma potential at the cathode and in the beam. If the beam is neutralized and wall effects eliminated, then this potential difference should be equivalent to the neutralizer voltage relative to ground.

In 1967 Hall et al. identified the need to either float the thruster chassis and plasma screen or to float the beam target to ensure an alternative neutralization pathway through the chamber walls does not arise¹⁰⁰. Some exploration into the impacts on beam neutralization of a floating beam target instead of floating the plasma screen has been briefly investigated by Topham et al.¹⁰¹. Other important considerations include the impact of stray external magnetic field



lines. They can terminate at nearby ground surfaces, or as discussed by Yu-Cai et al. can affect beam neutralization¹⁰². The field lines can provide a path for magnetized electrons to couple with the facility and alter neutralization pathways.

XIV. Concluding Remarks

Ion thruster technology remains a viable technology with the capacity for deep throttling making it equally applicable to interplanetary space science mission to human and cargo missions to Mars. It is also the most efficient of mature electric propulsion devices. Flexibility in operation is derived from the separation of beam acceleration and ion formation. Ion engine plasma generators which generate thrust producing ions can take many forms ranging from DC to electromagnetic coupling. Each of which have their own advantages ranging from thrust density to efficiency to lifetime. The document surveys basic operation of these various thrusters and more importantly the best practices for taking needed measurements to characterize the engines. This latter point cannot be overemphasized, to quantify operation one needs to know what measurements are relevant and how those measurements are implemented. Here we survey DC ion, microwave ion, and rf ion thrusters. These systems are mature embodiments and have space flight heritage. This document stands as a guide to the operation and characterization of these engines along with references that go into greater detail. It is critical that engine characterization is done in a manner that it can be compared to the existing body of knowledge. In this respect the document aims to serve as a source of basic core competency in characterizing these systems enabling further development keeping in mind those metrics that are required to quantify their operation. This document also surveys engine set up considerations which can introduce potential contamination as well as a means to gain engine insight without beam extraction. It is noted that this document is a survey, a portal to more details in the published literature; it is meant to also preserve basic knowledge of this operating this engine for generations to come.

Acknowledgments This work was partially supported by NASA through the Joint Advanced Propulsion Institute, a NASA Space Technology Research Institute, grant number 80NSSC21K1118. The research described in this paper was also carried out in part at the Jet Propulsion Laboratory, California Institute of Technology, under a contract with the National Aeronautics and Space Administration as well as JAXA and DLR.

References

- ¹ Beebe, D.D., Nakanishi, S., and Finke, R.C., "Electric Arc Discharge Damage to Ion Thruster Grids," Report No. NASA TM X-3044, May 1974.
- ² Pinero, L.R. and Rawlin, V.K., "Recycle Requirements for NASA's 30 cm Xenon Ion Thruster," *30th AIAA/SAE/ASME/ASEE Joint Propulsion Conference*, AIAA-1994-3303, Indianapolis, IN, June 27-29, 1994.
- ³ Martinez, R.A., Williams, J.D., and Goebel, D.M., "Electric Field Breakdown Properties of Materials Used in Ion Optics Systems," AIAA-2006-5004, *42nd Joint Propulsion Conference*, Sacramento, California, July 10–13, 2006.
- ⁴ Goebel, D.M., Katz, I., and Mikellides, I.G., "Fundamentals of Electric Propulsion, 2nd Edition," Chapter 4, Wiley, Inc., 2023.
- ⁵ Thomas, R.E., Raju, R.S., and Bontempo, J.J., "Characterizing Electrical Arc Behavior in Ion Engines," AIAA-2025-2041, *AIAA SciTech 2025 Forum*, Jan. 6-10, 2025
- ⁶ Goebel, D. M., and Schneider, A. C., "High-Voltage Breakdown and Conditioning of Carbon and Molybdenum Electrodes," *IEEE Transactions on Plasma Science*, Vol. 33, No. 4, 2005, pp. 1136–1148.
- ⁷ Diamant, K.D., Pollard, J.E., and Crofton, M.W., "Thrust Stand Characterization of the NASA NEXT Thruster," AIAA-2010-6701, *46th AIAA/ASME/SAE/ASEE Joint Propulsion Conference & Exhibit*, July 25-28, 2010.
- ⁸ Goebel, D.M., Katz, I., and Mikellides, I.G., "Fundamentals of Electric Propulsion, 2nd Edition," Chapter 2, Wiley, Inc., 2023.
- ⁹ Pollard, J.E., Diamant, K.D., Crofton, M.W., Patterson, M.J., "Spatially-Resolved Beam Current and Charge-State Distributions for the NEXT Ion Engine," AIAA-2010-6779, *46th AIAA/ASME/SAE/ASEE Joint Propulsion Conference & Exhibit*, July 25-28, 2010.
- ¹⁰ Snyder, J.S., Goebel, D.M., Hofer, R.R., Polk, J.E., Wallace, N.C., and Simpson, H., "Performance Evaluation of the T6 Ion Engine," *Journal of Propulsion and Power*, Vol. 28, No. 2 (2012).
- ¹¹ Aston, G., Kaufman, H.R., and Wilbur, P.J., "Ion Beam Divergence Characteristics of Two-Grid Accelerator Systems," *AIAA Journal*, Vol. 16, No. 5 (1978).
- ¹² Byers, D.C., "Angular Distribution of Kaufman Ion Thruster Beams," Report No. NASA TN D-5844 (1970).



The 39th International Electric Propulsion Conference, Imperial College London,
London, United Kingdom 14-19 September 2025

Page 43

Copyright 2025 by the Electric Rocket Propulsion Society. All rights reserved.

- ¹³ Rawlin, V.K., "Characterization of Ion Accelerating Systems on NASA LeRC's Ion Thrusters," AIAA-92-3827, *28th Joint Propulsion Conference and Exhibit*, July 6-8, 1992.
- ¹⁴ Wirz, R. and Goebel, D., "Effects of magnetic field topography on ion thruster discharge performance," *Plasma Sources Science and Technology*, Vol. 17 (2008).
- ¹⁵ Chen, J., Yanhui, J., Geng, H., Guo, N., and Guo, D., "Investigation of variable aperture on the performance and lifetime of ion thruster," *Plasma Science and Technology*, Vol. 23, No. 10 (2021).
- ¹⁶ Brophy, J.R., Katz, I., Polk, J.E., and Anderson, J.R., "Numerical Simulations of Ion thruster Accelerator Grid Erosion," AIAA-2002-4261, *38th AIAA/ASME/SAE/ASEE Joint Propulsion Conference & Exhibit*, July 7-10, 2002.
- ¹⁷ Arthur, N.A., "Ion Thruster Produced Roll Torque," AIAA-2019-4166, *AIAA Propulsion and Energy 2019 Forum*, Aug. 19-22, 2019.
- ¹⁸ Wartelsk, M., et al., "The Assessment of Interactions between Spacecraft and Electric Propulsion Systems Project," IEPC-2011-028, *32nd International Electric Propulsion Conference*, Sept. 11-15, 2011.
- ¹⁹ Fearn, G. D., "The Interactions Between a T5 Ion Thruster and a Host Spacecraft," ESA SP-398, *2nd European Spacecraft Propulsion Conference*, May 27-29, 1997.
- ²⁰ Samanta Roy, R.I., Hastings, D.E., and Gatsonis, N.A., "Numerical Study of Spacecraft Contamination and Interactions by Ion-Thruster Effluents," *Journal of Spacecraft and Rockets*, Vol. 33, No. 4 (1996).
- ²¹ Foster, J.E., Soulas, G.C., Patterson, M.J., "Plume and Discharge Plasma Measurements of an NSTAR-type Ion Thruster," AIAA-2000-3812, *36th Joint Propulsion Conference and Exhibit*, July 16-19, 2000.
- ²² Muhlich, N.S., Holste, K., Klar, P.J., and Leiter, H.J., "Near-field Beam Diagnostics for Radio-Frequency Ion Thrusters RIT," IEPC-2017-476, *35th International Electric Propulsion Conference*, Oct. 8-12, 2017.
- ²³ Tani, Y., Tsukizaki, R., Koda, D., Nishiyama, K., and Kuninaka, H., "Performance improvement of the μ 10 microwave discharge ion thruster by expansion of the plasma production volume," *Acta Astronautica* Vol. 157 (2019).
- ²⁴ Herman, D.A., Soulas, G.C., and Patterson, M.J., "Performance Evaluation of the Prototype Model NEXT Ion Thruster," AIAA-2007-5212, *43rd AIAA/ASME/SAE/ASEE Joint Propulsion Conference & Exhibit*, July 8-11, 2007.
- ²⁵ Farnell, C., Schmidt, M., Millot, R., Warner, D., Siler-Evans, K., and Williams, J., "Multi-Axis Plasma Profiling System for Characterization of Plasma Thruster Plumes," AIAA-2006-4818, *42nd AIAA/ASME/SAE/ASEE Joint Propulsion Conference & Exhibit*, July 9-12, 2006.
- ²⁶ Sheridan, T.E., "How Big is a Small Langmuir Probe?" *Physics of Plasmas*, Vol. 7, No. 7 (2000).
- ²⁷ Brown, D.L., Walker, M.L.R., Szabo, J., Huang, W., and Foster, J.E., "Recommended Practice for Use of Faraday Probes in Electric Propulsion Testing," *Journal of Propulsion and Power*, Vol. 33, No. 3 (2017).
- ²⁸ Polk, J.E., Anderson, J.R., Brophy, J.R., Rawlin, V.K., Patterson, M.J., Sovey, J., and Hamley, J., "An Overview of the Results from an 8200 Hour Wear Test of the NSTAR Ion Thruster," AIAA-99-2446, *35th Joint Propulsion Conference and Exhibit*, June 20-24, 1999.
- ²⁹ Thomas, R.E., et al., "Development of the Advanced NEXT High thrust-to-power Gridded Ion System," *Joint Army Navy NASA Air Force Interagency Propulsion Committee*, Oklahoma City, OK, May 6-10, 2024.
- ³⁰ Thomas, R. E., Gonzalez, M. C., Raju, R. S., Bontempo, J. J., Goodfellow, K. D., Aubuchon, C. A., Patterson, M. J., "Development Status and Performance Metrics of the Advanced NEXT Ion Propulsion System," IEPC-2025-133, *39th International Electric Propulsion Conference*, Sept 14-19, 2025.
- ³¹ Reynolds, T.W., "Mathematical Representation of Current Density Profiles from Ion Thrusters," Report No. NASA TN D-6334, April 1971.
- ³² Monheiser, J., et al., "A Summary of the NEXT-C Flight Thruster Proto-flight Testing," AIAA-2021-3408, *AIAA Propulsion and Energy 2021 Forum*, Aug. 9-11, 2021.
- ³³ Grubisic, A.N., Clark, S., Wallace, N., Collingwood, C., and Guarducci, F., "Qualification of the T6 Ion Thruster for the BepiColombo Mission to the Planet Mercury," IEPC-2011-234, *32nd International Electric Propulsion Conference*, Sept. 11-15, 2011.
- ³⁴ Rafalskyi, D., et al. "In-orbit demonstration of an iodine electric propulsion system," *Nature*, Vol. 599 (2021).
- ³⁵ Habi, L., Rafalskyi, D., and Lafleur, T., "Ion beam diagnostic for the assessment of miniaturized electric propulsion systems," *Review of Scientific Instruments*, Vol. 91., Issue 9 (2020).
- ³⁶ Pollard, J.E., Diamant, K.D., Crofton, M.W., Patterson, M.J., "Spatially-Resolved Beam Current and Charge-State Distributions for the NEXT Ion Engine," AIAA-2010-6779, *46th AIAA/ASME/SAE/ASEE Joint Propulsion Conference & Exhibit*, July 25-28, 2010.
- ³⁷ Young, J.A., Matlock, T.S., Nakles, M., Crofton, M.W., Patterson, M.J., Arthur, N., and John, J.W., "Far Field Plume Distribution and Divergence for NEXT: DART Mission," AIAA 2019-1243, *2019 AIAA Scitech Forum*, January 7-11, 2019.
- ³⁸ Snyder, J.S., Goebel, D.M., Hofer, R.R., Polk, J.E., Wallace, N.C., and Simpson, H., "Performance Evaluation of the T6 Ion Engine," *Journal of Propulsion and Power*, Vol. 28, No. 2 (2012).



The 39th International Electric Propulsion Conference, Imperial College London,
London, United Kingdom 14-19 September 2025

Page 44

Copyright 2025 by the Electric Rocket Propulsion Society. All rights reserved.

- ³⁹ Soulas, G.C., Foster, J.E., and Patterson, M.J., "Performance of Titanium Optics on a NASA 30 cm Ion Thruster," *AIAA-2000-3814, 36th AIAA/ASME/SAE/ASEE Joint Propulsion Conference and Exhibit*, July 17-29, 2000.
- ⁴⁰ Porst, J.-P., et al., "The RIT 2X propulsion system: current development status," IEPC-2017-505, *35th International Electric Propulsion Conference*, Oct. 8-12, 2017.
- ⁴¹ Vahrenkamp, R.P., "Measurement of Double Charged Ions in the Beam of a 30 cm Mercury Bombardment Thruster," AIAA-73-1057, *AIAA 10th Electric Propulsion Conference*, Oct. 31 – Nov 2, 1973.
- ⁴² Bundesmann, C., et al., "An advanced electric propulsion diagnostic (AEPD) platform for in-situ characterization of electric propulsion thrusters and ion beam sources," *The European Physical Journal D*, Vol. 70, No. 212 (2016).
- ⁴³ Mundy, D., "T5 Ion Engine Plume Analysis using a Time of Flight Mass Spectrometer," IEPC-97-096, *25th International Electric Propulsion Conference*, Aug. 24-28, 1997.
- ⁴⁴ Pollard, J.E., "Plume Measurements with the T5 Xenon Ion Thruster," AIAA-94-3139, *30th AIAA/ASME/SAE/ASEE Joint Propulsion Conference*, June 27-29, 1994.
- ⁴⁵ Rovey, J.L., "Recommended Practice for Use of ExB Probes in Electric Propulsion Testing," *39th International Electric Propulsion Conference*, Sept 14-19, 2025.
- ⁴⁶ Brophy, J.R., et al., "Numerical Simulations of Ion Thruster Accelerator Grid Erosion," AIAA-2002-4261, *38th AIAA/ASME/SAE/ASEE Joint Propulsion Conference & Exhibit*, July 7-10, 2002.
- ⁴⁷ Shastry, R., Herman, D.H., Soulás, G.C., and Patterson, M.J., "End-of-test Performance and Wear Characterization of NASA's Evolutionary Xenon Thruster (NEXT) Long-Duration Test," AIAA-2014-3617, *50th AIAA/ASME/SAE/ASEE Joint Propulsion Conference*, July 28-30, 2014.
- ⁴⁸ Herman, D.H., Soulás, G.C., and Patterson, M.J., "Performance Evaluation of the Prototype-Model NEXT Ion Thruster," AIAA-2007-5212, *43rd AIAA/ASME/SAE/ASEE Joint Propulsion Conference & Exhibit*, July 8-11, 2007.
- ⁴⁹ Soulás, G.C., and Patterson, M.J., "NEXT Ion Thruster Performance Dispersion Analyses," AIAA-2007-5213, *43rd AIAA/ASME/SAE/ASEE Joint Propulsion Conference & Exhibit*, July 8-11, 2007.
- ⁵⁰ Rawlin, V.K., et al., "NSTAR Flight Thruster Qualification Testing," AIAA-1998-3936, *34th AIAA/ASME/SAE/ASEE Joint Propulsion Conference and Exhibit*, 1998.
- ⁵¹ Rawlin, V.K., "Characterization of Ion Accelerating Systems on NASA LeRC's Ion Thrusters," AIAA-1992-3827, *AIAA/ASME/SAE 28th Joint Propulsion Conference and Exhibit*, July 6-8, 1992.
- ⁵² Rovang, D.C., and Wilbur, P.J., "Ion Extraction Capabilities of Two-Grid Accelerator Systems," *Journal of Propulsion and Power*, vol. 1, no. 3, May-June, 1985, pp. 172-179.
- ⁵³ Sengupta, A., et al., "Status of the Extended Life Test of the Deep Space 1 Flight Spare Ion Engine After 30,352 Hours of Operation," AIAA-2003-4558, *39th AIAA/ASME/SAE/ASEE Joint Propulsion Conference and Exhibit*, July 20-23, 2003.
- ⁵⁴ Williams, J.D., Goebel, D.M., and Wilbur, P.J., "Analytical Model of Electron Backstreaming for Ion Thrusters," AIAA-2003-4560, *39th AIAA/ASME/SAE/ASEE Joint Propulsion Conference and Exhibit*, July 21-23, 2003.
- ⁵⁵ Diaz, E.M. and Soulás, G.C., "Grid Gap Measurement for an NSTAR Ion Thruster," IEPC-2005-244, *29th International Electric Propulsion Conference*, October 31-November 4, 2005.
- ⁵⁶ Pollard, J.E. and Welle, R.P., "Thrust Vector Measurements with the T5 Ion Engine," AIAA Paper 95-2829, *31st AIAA/ASME/SAE/ASEE Joint Propulsion Conference and Exhibit*, July 10-12, 1995.
- ⁵⁷ Kaufman, H. R., "Ion-Thruster Propellant Utilization," *NASA Technical Note*, NASA TN D-6591, Washington, D. C., December 1971.
- ⁵⁸ Herman, D. A., Soulás, G. C., and Patterson, M. J., "Performance Characteristics of the NEXT Long-Duration Test after 16,550 h and 337 kg of Xenon Processed," *44th AIAA/ASME/SAE/ASEE Joint Propulsion Conference & Exhibit*, AIAA 2008-4527, Hartford, CT, July 21-23, 2008.
- ⁵⁹ Goebel, D. M., and Katz, I., "Fundamentals of Electric Propulsion: Ion and Hall Thrusters," *JPL Space Science and Technology Series*, Jet Propulsion Laboratory, California Institution of Technology, March, 2008.
- ⁶⁰ Snyder, J., Goebel, D., Hofer, R., Polk, J., Wallace, N., and Simpson, H., "Performance Evaluation of the T6 Ion Engine," AIAA 2010-7114, *46th AIAA/ASME/SAE/ASEE Joint Propulsion Conference & Exhibit*, July 25-28, 2010.
- ⁶¹ Polk, J., Anderson, J., Brophy, J., Rawlin, V., Patterson, M., Sovey, J., and Hamley, J., "An Overview of the Results from an 8200 Hour Wear Test of the NSTAR Ion Thruster," AIAA 1999-2446, *35th Joint Propulsion Conference and Exhibit*, June 20-24, 1999.
- ⁶² Polk, J., Anderson, J., and Brophy, J., "Behavior of the Thrust Vector in the NSTAR Ion Thruster," AIAA 1998-3940, *34th AIAA/ASME/SAE/ASEE Joint Propulsion Conference and Exhibit*, July 13-15, 1998.
- ⁶³ Benavides, G. F., Mackey, J., Ahern, D., and Thomas, R., "Diagnostic for Verifying the Thrust Vector Requirement of the AEPS Hall-Effect Thruster and Comparison to the NEXT-C Thrust Vector Diagnostic," AIAA 2018-4514, *2018 Joint Propulsion Conference*, July 9-11, 2018.



- ⁶⁴ J. R. Brophy, "Simulated Ion Thruster Operation Without Beam Extraction," AIAA 1990-2655, *AIAA/DGLR/JSASS, 21st International Electric Propulsion Conference*, July 18-20, 1990.
- ⁶⁵ D. Goebel, J. Polk, and A. Sengupta, "Discharge Chamber Performance of the NEXIS Ion Thruster," AIAA 2004-3813, *40th AIAA/ASME/SAE/ASEE Joint Propulsion Conference and Exhibit*, 11-14 July 2004.
- ⁶⁶ J. E. Foster, et al, "Simulated Beam Extraction Performance Characterization of a 50-cm Ion Thruster Discharge," AIAA 2012-3795, *48th AIAA/ASME/SAE/ASEE Joint Propulsion Conference & Exhibit*, 30 July - 01 August 2012.
- ⁶⁷ K. Nishiyama, S. Hosoda, R. Tsukizaki, and H. Kuninaka, "In-flight operation of the Hayabusa2 ion engine system on its way to rendezvous with asteroid 162173 Ryugu", *Acta Astronautica*, Vol. 166, (2020), pp. 69-77, doi: 10.1016/j.actaastro.2019.10.005
- ⁶⁸ Yoshimoto, S., Nakasuka, S., Tsuruda, Y., Aoyanagi, Y., Tanaka, T., Sahara, H., Ohira, T., Araki, Y., Mase, I., Ito, M., Kainov, V., Karandaev, A., and Silkin, O., "Cluster Launch of Hodoyoshi-3 and -4 Satellites from Yasny by Dnepr Launch Vehicle," *Transactions of the Japan Society for Aeronautical and Space Sciences, Aerospace Technology Japan*, Vol. 14, No. ists30, 2016, pp. Pf_35-Pf_43. doi:10.2322/tastj.14.Pf_35
- ⁶⁹ Funase, R., Koizumi, H., Nakasuka, S., Kawakatsu, Y., Fukushima, Y., Tomiki, A., Kobayashi, Y., Nakatsuka, J., Mita, M. and Kobayashi, D., "50kg-Class Deep Space Exploration Technology Demonstration Micro-spacecraft PROCYON", 28th Annual AIAA/USU Conference on Small Satellites, Utah State University, 2-7 August 2014.
- ⁷⁰ Ryudo Tsukizaki, Toshiyuki Ise, Hiroyuki Koizumi, Hiroyoshi Togo, Kazutaka Nishiyama, and Hitoshi Kuninaka., Thrust Enhancement of a Microwave Ion Thruster, *Journal of Propulsion and Power*, Vol. 30, No. 5 (2014), pp. 1383-1389. doi: 10.2514/1.B35118
- ⁷¹ Yoshitaka Tani, Ryudo Tsukizaki, Daiki Koda, Kazutaka Nishiyama, and Hitoshi Kuninaka, Performance improvement of the μ10 microwave discharge ion thruster by expansion of the plasma production volume, *Acta Astronautica*, Vol. 157, (2019), pp. 425-434
- ⁷² Yoshitaka Tani, Yusuke Yamashita, Ryudo Tsukizaki, Kazutaka Nishiyama, Hitoshi Kuninaka, Effect of discharge chamber geometry on ion loss in microwave discharge ion thruster, *Acta Astronautica*, Volume 176, 2020, Pages 77-88, ISSN 0094-5765, <https://doi.org/10.1016/j.actaastro.2020.05.062>.
- ⁷³ Yoshitaka Tani, Experimental Investigation of the Effect of Magnetic Field Geometry on the Microwave Discharge Ion Thruster Performance, Ph.D dissertation, The university of Tokyo, 2019, <https://repository.dl.itc.u-tokyo.ac.jp/record/2001968/files/A35812.pdf>
- ⁷⁴ Ryudo Tsukizaki, Yuta Yamamoto, Daiki Koda, Yamashita Yusuke, Kazutaka Nishiyama and Hitoshi Kuninaka, Azimuthal velocity measurement in the ion beam of a gridded ion thruster using laser-induced fluorescence spectroscopy, *2018 Plasma Sources Sci. Technol.* 27 015013
- ⁷⁵ Yusuke, YAMASHITA, Ryudo TSUKIZAKI, Yuta YAMAMOTO, Daiki KODA, Kazutaka, NISHIYAMA, and Hitoshi KUNINAKA, Azimuthal ion drift of a gridded ion thruster, *Plasma Sources and Science Technology*, Vol.27,(2018), 10, p.5006-5014
- ⁷⁶ Kazutaka, Nishiyama, et al., proceedings of Space Transportation Symposium 2011, [\(in Japanese\)](https://www.isas.jaxa.jp/j/researchers/symp/ss11/paper/P3-087_20110208170511.pdf)
- ⁷⁷ Hitoshi Kuninaka, et al, Powered flight by ion engine, Corona, ISBN 978-4-339-01228-6, 2006, [\(in Japanese\)](https://www.coronasha.co.jp/np/isbn/9784339012286/)
- ⁷⁸ Takato Morishita, Ryudo Tsukizaki, Kazutaka Nishiyama, Hitoshi Kuninaka, Plasma parameters measured inside and outside a microwave-discharge-based plasma cathode using laser-induced fluorescence spectroscopy,, *Journal of Applied Physics*, (2022), doi: 10.1063/5.0071294
- ⁷⁹ Goebel, D. M., Katz, I., "Fundamentals of Electric Propulsion". United Kingdom: Wiley, 2008, doi: 10.1002/9780470436448
- ⁸⁰ Polk, J., Chaplin, V., Anderson, J., Yim, J., Soulard, G., Williams, G., Shastry, R., "Modeling grid erosion in the NEXT ion thruster using the CEX2D and CEX3D codes". *Journal of Electric Propulsion*, 2,1 (2023) 14, doi: 10.1007/s44205-023-00043-0
- ⁸¹ Becker, R., Herrmannsfeldt, W. B., "igun-A program for the simulation of positive ion extraction including magnetic fields". *Review of Scientific Instruments* **63**,4 (1992) 2756, doi: 10.1063/1.1142795
- ⁸² Kalvas, T., Tarvainen, O., Ropponen, T., Steczkiewicz, O., Årje, J., Clark, H., "IBSIMU: A three-dimensional simulation software for charged particle optics." *Review of Scientific Instruments* **81**,2 (2010) 02B703, doi: 10.1063/1.3258608
- ⁸³ Tartz, M., Hartmann, E., Neumann, H., "Validated simulation of the ion extraction grid lifetime". *Review of Scientific Instruments*, **79** (2008) 02B905, doi: 10.1063/1.2801376
- ⁸⁴ Boré, A., et al., "Improved control architecture and strategy for iodine ion thruster following in-orbit demonstration and system-level radiation testing," *Journal of Electric Propulsion*, Vol 2, Article 7 (2023). <https://doi.org/10.1007/s44205-023-00041-2>
- ⁸⁵ Tsay, M., et al., "Neutralization Demo and Thrust Stand Measurement for BIT-3 RF Ion Thruster," 2017 AIAA Propulsion and Energy Forum, Atlanta, GA, July 2017, AIAA-2017-4890.
- ⁸⁶ Holkeboer, D. H., Vacuum Technology and space simulation, American Institute of Physics, 1993.
- ⁸⁷ Szalai, Kenneth J. et al., "TSS-1R Mission Failure Investigation Board: Final Report," NASA-TM-112426, 1996.



- ⁸⁸ A. A. P., Chaudhuri, P., Khirwadkar, S., Chauhan, N., Raole, P. M., Reddy, D. C., and Saxena, Y. C., "On Residual Gas Analysis during High Temperature Baking of Graphite Tiles," *Journal of Physics: Conference Series*, Vol. 114, 2008, p. 012063. <https://doi.org/10.1088/1742-6596/114/1/012063>
- ⁸⁹ A. Sengupta, J. A. Anderson, C. Garner, J. R. Brophy, K. K. de Groh, B. A. Banks and T. A. K. Thomas, "Deep space 1 flight spare ion thruster 30,000-hour life test," *Journal of Propulsion and Power*, vol. 25, no. 1, pp. 105--117, 2009.
- ⁹⁰ R. Shastry, D. A. Herman, G. C. Soulard and M. J. Patterson, "Status of NASA's Evolutionary Xenon Thruster (NEXT) long-duration test as of 50,000 h and 900 kg throughput," in *International Electric Propulsion Conference (IEPC)*, 2015.
- ⁹¹ J. Wang, O. Chang and Y. Cao, "Electron–ion coupling in mesothermal plasma beam emission: Full particle PIC simulations," *IEEE transactions on plasma science*, vol. 40, no. 2, pp. 230--236, 2012.
- ⁹² C. Lipscomb, I. D. Boyd, K. B. Hansson, J. Eckels and A. Gorodetsky, "Simulation of Vacuum Chamber Pressure Distribution with Surrogate Modeling and Uncertainty Quantification," in *AIAA SCITECH 2024 Forum*, 2024.
- ⁹³ J. Yim and J. M. Burt, "Characterization of vacuum facility background gas through simulation and considerations for electric propulsion ground testing," in *51st AIAA/SAE/ASEE Joint Propulsion Conference*, 2015.
- ⁹⁴ E. Taghizadeh, R. A. Obenchain, L. K. Franz and R. E. Wirz, "Electric Propulsion Facility Optimization via Reduced," in *38th International Electric Propulsion Conference*, Toulouse, France, 2024.
- ⁹⁵ J. W. Dankanich, M. Walker, M. W. Swiatek and J. T. Yim, "Recommended practice for pressure measurement and calculation of effective pumping speed in electric propulsion testing," *Journal of Propulsion and Power*, vol. 33, no. 3, pp. 668--680, 2017.
- ⁹⁶ T. J. Topham and U. o. M. N. E. & R. Sciences, Understanding the Mechanisms Affecting Gridded Ion Engine Operation in Ground Test Facilities, Ann Arbor: ProQuest Dissertations & Theses, 2025.
- ⁹⁷ M. Patterson and T. Verhey, "5kW xenon ion thruster lifetest," in *21st International Electric Propulsion Conference*, 1990.
- ⁹⁸ T. Topham and J. Foster, "Characterization of the effect of plasma screen electrical configuration on gridded ion engine operation," in *Bulletin of the American Physical Society*, 2023.
- ⁹⁹ T. J. Topham, S. Bergmann, A. C. A. Almeida and J. E. Foster, "Impacts of thruster chassis potential on beam neutralization at high-power densities," in *39th International Electric Propulsion Conference*, Imperial College London, 2025.
- ¹⁰⁰ D. Hall, R. Kemp and H. Shelton, "Mercury discharge devices and technology," in *6th Electric Propulsion and Plasmadynamics Conference*, 1967.
- ¹⁰¹ T. J. Topham, S. E. Bergmann, A. C. Alves Almeida, J. A. Judge and J. E. Foster, "Evaluation of Facility Effect Impacts on Gridded Ion Engines at High Power Densities," in *AIAA SCITECH 2025 Forum*, Orlando, 2025.
- ¹⁰² F. Yu-Cai and P. J. Wilbur, "The influence of stray magnetic fields on ion beam neutralization," in *16th International Electric Propulsion Conference*, 1982.

